Chapter 1
Structure Concepts in Two-Dimensional Oxide Materials

Falko P. Netzer and Svetlozar Surnev

Abstract The atomic structures of two-dimensional oxide systems are investigated with the aim to unravel trends in their complex structural behavior and to identify the major structure-determining descriptors. Categories of oxide structures are introduced, and the important role of the various degrees of freedom of the metal-oxide interface parameters for 2-D structure formation and stability is highlighted with the help of prototypical examples.

1.1 Introduction

Ultrathin films of metal oxides constitute a new class of materials, whose properties deviate from and are often not shared by their respective bulk counterparts [1, 2]. The film thicknesses, at which these deviations from bulk behavior occur, are not uniquely defined and may depend on the particular material and on the physical or chemical properties under consideration. In this chapter, we will be very restrictive and address oxide "films" that are at the two-dimensional (2-D) limit, i.e. oxide materials consisting of only one atomic layer or one single-polyhedron thick layer. In this limit of single layers, the behavior of the oxides approaches that of true 2-D systems. For practical and experimental purposes, the oxide monolayers are typically supported on a solid substrate: convenient substrates are metal single crystal surfaces. The surface science of metal single crystal surfaces is well established, they are easy to prepare in atomically clean form, and their conducting character is beneficial for the use of experimental methodologies involving charged particle probes. Of course, oxide monolayers on metal single crystal surfaces cannot be considered as systems of practical reality, but have to be regarded as model systems

F.P. Netzer (✉) · S. Surnev
Surface and Interface Physics, Institute of Physics, Karl-Franzens University Graz, Universitätsplatz 5, 8010 Graz, Austria
e-mail: falko.netzer@uni-graz.at

S. Surnev
e-mail: svetlozar.surnev@uni-graz.at

F.P. Netzer and A. Fortunelli (eds.), *Oxide Materials at the Two-Dimensional Limit*, Springer Series in Materials Science 234, DOI 10.1007/978-3-319-28332-6_1

for fundamental studies of scientific endeavor. Studies on model systems are an inherent and essential component of the scientific analytical approach. They allow for a close coupling of experiments with theory, thus creating a platform for a detailed atomic understanding of the properties in low-dimensional complex solids.

The science of 2-D materials has seen a veritable hype during the last decade, which was prompted by the discovery of graphene, and many 2-D materials beyond graphene have been introduced since [3]. Most of these 2-D materials are derived from *van der Waals* solids, that are layered solids characterized by strong intra-layer but weak inter-layer interactions; the latter occur because the layers are internally bond saturated. When depositing these 2-D layers on a substrate, the overlayer-substrate interactions are typically weak. This is in contrast to oxides supported on metal surfaces, where strong interfacial interactions are often encountered, in particular in the case of transition metal oxide overlayers. This strong interfacial coupling of a nanoscale oxide to a metal surface creates a new combined system, an oxide-metal hybrid system, with novel and often unprecedented physical and chemical properties as compared to its individual constituents [4–6]. For oxide overlayers at the 2-D limit, the behavior of the oxide-metal hybrid system is largely determined by the interactions at the interface: in a way, a 2-D oxide layer on a metal may be regarded as a model system or even as an expression of the true oxide-metal interface.

Several degrees of freedom contribute to the interfacial interactions, amongst them structural, electronic and chemical, corresponding to the atomic geometry, the mixing of electronic energy levels including charge transfer, and to the chemical bonding at the interface. In this chapter, we will concentrate on the aspects of atomic structure, which is a key property to which many other properties are related. In a formally reductionist approach, the influence of parameters such as lattice (mis)match and symmetry, electronic effects as well as chemical affinities and bonding at the interface on the oxide overlayer structure will be treated separately, keeping however in mind the interplay and the intricately interwoven balance of these parameters in determining the atomic geometry of the 2-D oxide layer. Structure concepts in 2-D will be highlighted in comparison to bulk structure motifs, and the effects of stabilizing particular structures in 2-D, such as polarity compensation, strain release, charge transfer and finite size effects will be identified. The chemical bonding at the interface as a result of the local epitaxial relationship and the influence of the surface energy and the adhesion energy of the overlayer in the total energy balance [7] will also be points of discussion.

Bulk oxide structures may be visualized from two different viewpoints: (i) as a stacking sequence of layers, for example the rock salt structure in [111] direction can be seen as a sequence of alternating hexagonal planes of oxygen (anions) and metal atoms (cations) (Fig. 1.1a); or (ii) as the combination of metal-oxygen polyhedral coordination blocks, connected and nested via shared corners, edges and planes of the polyhedra; the cubic arrangement of metal-oxygen octahedra in the ReO_3 structure (the parent structure of the perovskite oxides) via the connection of corners is an example for the latter (see Fig. 1.1b). The 2-D structures discussed here will be categorized accordingly, trying to use the most intuitive and pictorial

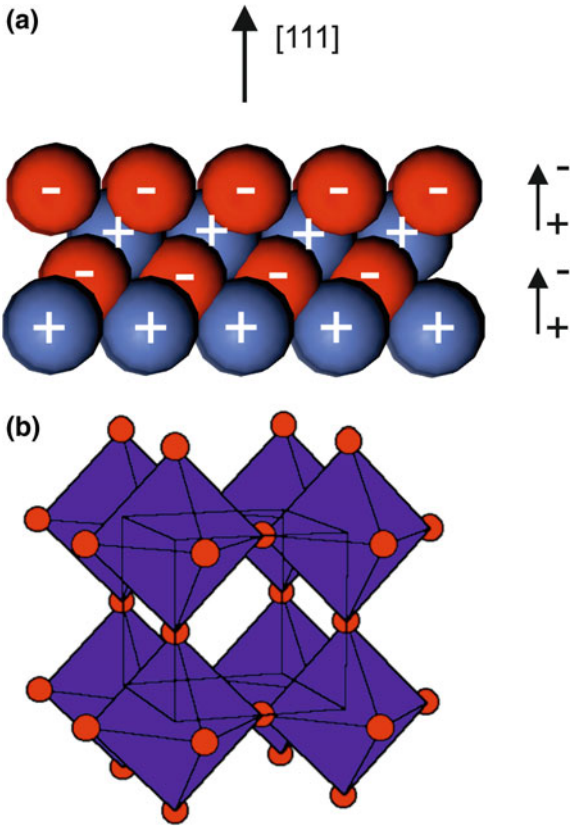

Fig. 1.1 **a** Representation of the rock salt structure (RS) as a stack of hexagonal cation and anion layers in the [111] direction. **b** Cubic ReO_3 structure, consisting of corner sharing ReO_6 octahedra (*red* O atoms) (Color figure online)

representation for the description. The chemistry at the interface depends on the affinities of the involved elements to each other and to oxygen. The interfacial interactions may be divided into strong and weak, creating so called reactive interfaces, with interdiffusion or chemical reaction of the constituents, or non-reactive and abrupt interfaces, respectively. If the metal surface is intended to provide mainly a rigid support for the 2-D oxide layer, noble metal surfaces of group VIII or Ib are typically chosen, thus providing abrupt, but not necessarily chemically inert interfaces. In the case of weak oxide-metal interactions, incommensurate oxide overlayers are frequently observed. They lead to characteristic patterns in the low-energy electron diffraction (LEED) diagrams or in scanning tunneling microscopy (STM) images due to the Moiré superposition effect of mismatched lattices and are easily identified, as discussed further below. Subtle variations of the interface chemistry modify the oxide-metal hybrid system and allow one to tune some of the properties to a certain extent: for a given oxide overlayer, completely different structure concepts may be encountered on different metal substrate surfaces. However, also here the intermixing and balance of geometrical, electronic and chemical degrees of freedom may be pronounced.

External thermodynamic parameters during the fabrication of 2-D oxide systems such as temperature and oxygen pressure, i.e. the chemical potential of oxygen μ_O, have a profound influence on the stoichiometry and the oxidation state of the growing oxide phase. It has to be mentioned that most experimental investigations of 2-D oxide systems employ the so called surface science approach, that is preparation using physical vapor deposition methods in ultrahigh vacuum (UHV) and in situ characterization of the oxide deposits [8, 9]. Thin film growth is inherently a non-equilibrium kinetic process. However, kinetic effects leading to the stabilization of meta-stable oxide structures tend to be more important in 2-D than in the 3-D case, as a result of more flexibility in the structural components and in phase composition. The discussion of 2-D oxide phase diagrams will give an impression of phase complexities in some oxide-metal systems and of the interplay between thermodynamic versus kinetic effects.

As argued above, 2-D oxides on metal surfaces are interesting model systems for the study of the emergent properties of low-dimensional solids, however quasi-2-D oxide layers exist already in a number of present-day technologies, and promising applications in new device elements of the upcoming nanotechnologies may be envisioned. 2-D oxides are used as catalytic materials, in solid oxide fuel cells and gas sensors, as corrosion protection layers, and in nano-electronic and spintronic devices [10]. As multifunctional systems, they are of interest in biocompatibility applications, in solar energy cells and the multi-ferroic properties of some oxide systems may eventually be used for novel ways of information storage. Turning on to a different subject, the particular geometry of 2-D oxide layers at the interface between metal substrate and oxide overlayer phases is important in mediating the epitaxial growth of oxide thin films. The flexibility of their low-dimensional structures may provide graded interfaces between dissimilar substrate and film materials and may thus enable the epitaxial growth by adjusting symmetry and lattice mismatch. The fields of interest and applications of 2-D oxide systems are thus diverse and wide open and new developments yet unforeseen may well be at hand.

The organization of this chapter is as follows. In Sect. 1.2, 2-D structure categories are introduced, which allow us to identify common trends in the complex variety of oxide-metal systems. The various structure types will be introduced and analysed in the different subsections. In Sect. 1.3, the focus is on the reactivity of interfaces, and this will lead us on the road of increasing complexity from binary oxides to ternary oxide layers. In Sect. 1.4, we address finite size effects in stabilizing 2-D oxide structures, whereas in Sect. 1.5 the influence of the interface chemistry in terms of the affinities of the chemical constituents of the interface on the 2-D oxide structure type is examined. In Sect. 1.6, the thermodynamic stability and kinetic effects of formation of 2-D oxide structures is at the basis of the presented surface phase diagrams. Here, a selected 2-D oxide phase diagram in the form of a projection of the stability regions of phases onto the relevant parameter space is discussed. In Sect. 1.7, the role of the interface bonding subjected to the local epitaxial relationship in lattice and symmetry mismatched systems, leading to mesoscopic nanopattern formation, is investigated. Finally, a brief synopsis in Sect. 1.7 concludes the chapter. Throughout the sections, it is attempted to identify

benchmark or prototypical oxide-metal systems to illustrate the 2-D structure concepts and their major stabilizing agents: within the framework of the reductionist approach these are the release or minimization of strain, the compensation of polarity, electronic charge transfer and local bonding at the interface, which will be conceptually treated as separate effects. As the focus of this chapter is on concepts, a comprehensive bibliographic referencing by listing the available information of reported oxide-metal systems according to their structure types is not undertaken.

1.2 Structure Elements of 2-D Oxide Systems on Metal Surfaces

The cubic rock salt structure (RS), which is the structural basis of the stable 3d transition metal (TM) monoxides VO, MnO, FeO, CoO and NiO, provides a useful starting ground for deriving structure elements of 2-D oxide systems. Many different structure motifs of 2-D oxides can be created by and related to simple RS structure blocks, with modifications as a result of interface and dimensionality effects. The most stable surface of RS is the non-polar (100) plane, which is a square arrangement of oxygen anions and metal cations in a single charge compensated plane. Planar oxide monolayers of RS (100)-type with square symmetry and modifications or reconstructions thereof provide stable structures for a number of TM oxide systems (see Sect. 1.2.1). The hexagonal monolayer analog of the RS (100) plane is not a structure element of RS, but it can be derived from the hexagonal boron nitride (BN) structure, by replacing B and N by metal and oxygen. Indeed, this structure has been found for some 2-D oxide layer systems. Uniaxial structure motifs, with two-fold symmetry properties, have also been observed in planar, or quasi-planar oxide single layers—the latter display a weak corrugation or rumpling of anion or cation sites in a preferred direction, but the deviation from planarity is less than in the bilayer structures mentioned below. Uniaxial structure formation requires a change of lattice symmetry across the interface (e.g. a hexagonal overlayer lattice on a square substrate) or the presence of local metal-oxygen (M–O) coordination spheres of different type, e.g. square and triangular units, within the overlayer (also discussed in Sect. 1.2.1).

In [111] direction, the RS consists of stacks of hexagonal bilayers of oxygen and metal planes (see Fig. 1.1a). These bilayers are polar, with a finite dipole moment perpendicular to the planes, and they are unstable in the bulk due to a diverging electrostatic energy, unless there is charge compensation at the surfaces [11, 12]. In 2-D, however, they may become stable structure elements, because additional mechanisms of polarity compensation become operative. Hexagonal O–M–O trilayer structures may also be derived from the [111] RS stacking sequence: they are stable charge compensated unpolar slabs and have been observed to form on several

2-D oxide systems at higher chemical potentials of oxygen, i.e. under more severe oxidizing conditions. The bilayer and trilayer structures are analyzed in Sect. 1.2.2.

More complex 2-D structures, comprising different connectivities of M–O building blocks and metal cations with different oxygen coordination spheres, and thus different oxidation states, have been detected for the early TM oxides, such as Ti and V oxides; this is the reflection of the comparable stability of different oxidation states of the metal cations. In Sect. 1.2.3, examples of such oxide systems with complexity in oxidation states are introduced and discussed. Furthermore, the formation of complicated quasi-2-D networks of alumina with unusual Al–O surroundings is mentioned here.

Elastic strain, as a result of the epitaxial lattice mismatch at the interface, and its reduction is an important issue in oxide overlayer structure considerations. In 2-D systems, the strain term in the total energy balance may become a decisive factor in promoting novel structure elements that are not stable in 3-D bulk systems. It is therefore appropriate at this point to recall some basic facts. The lattice mismatch **m** is defined by

$$\mathbf{m} = (\mathbf{b} - \mathbf{a})/\mathbf{a} \tag{1.1}$$

with **b** the lattice constant of the overlayer and **a** that of the substrate. Traditionally, the lattice constants of the bulk systems have been taken to evaluate **m** [13, 14]. While this is a reasonable approximation for the substrate surface, it is not so for the 2-D overlayer. The lattice constant of an isolated 2-D layer is contracted with respect to the bulk value. In a somewhat hand-waving argument, this may be understood by the picture of bond strength conservation involving the coordination number [15]: a M–O dimer has a smaller bond length than a 2-D M–O layer, which in turn has smaller bond lengths than the 3-D solid, in sympathy with the increase of the coordination number. Thomas and Fortunelli [16] have investigated, using a density functional DFT + U method, the lattice parameter of NiO(100) on Ag(100) and have compared it to the free standing NiO monolayer. Accordingly, the isolated NiO monolayer has a Ni–Ni spacing of 2.8 Å, which is shrinked by approximately 5 % from the experimental NiO bulk value (2.95 Å). If the NiO monolayer is deposited on a metal surface, the oxide-metal bonding increases the coordination number again and the contraction is partly reversed. The calculations predict that a NiO monolayer on Ag(100) is compressed by 2 %, whereas on Pd(100) a compression of NiO of 3.6 % is predicted [17]. The interfacial strain is thus significantly smaller than the 7 % estimate based on the lattice mismatch as calculated using the respective bulk lattice constants. Thus, in some formally strongly lattice mismatched overlayer-substrate systems—if using bulk lattice parameters for the estimate—the actual lattice mismatch and the corresponding strain can be much less, if the low dimensionality of the overlayer is taken into account.

1.2.1 Planar Oxide Monolayers

Here the term "planar" is used to indicate that the metal and oxygen atoms are located essentially in a single plane, although the surface does not necessarily have to be completely flat, but can be corrugated or rumpled, with the centre of gravity of the anion or cation species slightly offset. Of course, the distinction between single layer and bilayer, where anions and cations are considered to belong to separate *layers*, is somewhat arbitrary, but so is the entire categorization, which is merely a pedagogical construct to facilitate the discussion. In the first part of this subsection, oxide single layer structures that can be derived from a RS (100)-type plane are investigated.

RS (100)-type structures. The simplest structure motif in this context is a single (100) plane of a metal oxide with monoxide MO stoichiometry. This geometry is adopted by the NiO(100)1 × 1 monolayer phase on Ag(100) [18, 19]. Figure 1.2 presents STM images of a NiO(100)1 × 1 island on Ag(100), obtained from a surface prepared by deposition of 2/3 of a monolayer of Ni in 1×10^{-6} mbar O_2 on the Ag surface at room temperature followed by annealing at 600 K in oxygen. The NiO island in Fig. 1.2a shows a morphology reflecting the square symmetry of the (100) plane, whereas the high resolution image in Fig. 1.2b reveals the square mesh of bright protrusions, which have been associated with the Ni atoms according to the DFT calculations [18]. The NiO surface displays a mosaic pattern of brighter and darker contrast regions (Fig. 1.2a). This has been interpreted in terms of local regions, where the NiO forms patches of a bilayer structure, with the brighter STM contrast stemming from the monolayer and the darker from the bilayer regions. The formation of bilayer patches is a way to release the residual interfacial strain—we recall from above that the NiO monolayer is 2 % contracted on the Ag(100). The bilayer has a slightly expanded lattice (due to the higher coordination) and thus improves the elastic energy balance. The darker contrast in the STM image of the bilayer region is due to the lower density of states around the Fermi energy of the

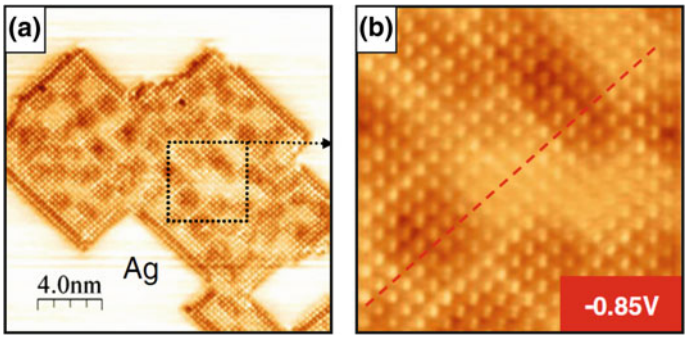

Fig. 1.2 STM images of a NiO(100)1 × 1 island embedded in Ag(100). **a** (20 × 20 nm^2); sample bias voltage V_S = −0.85 V; tunneling current I_T = 0.5 nA. **b** (5 × 5 nm^2); V_S = −0.85 V; I_T = 0.5 nA; image FFT filtered. Adapted from [19]

bilayer as compared to the monolayer, which is metallic as a result of the interaction with the metal surface [16, 18, 19]. The NiO island in Fig. 1.2 is embedded into the Ag substrate rather than located on top, and this is the majority configuration on this surface. The DFT calculations [18] have found that the embedded (1 × 1) monolayer structure gains stability by the Ni–Ag bonding and the formation of a bilayer rim at the island boundaries. Figure 1.3 gives a schematic model of a NiO(100)1 × 1 island embedded into the Ag(100) surface. In this context, it is of interest to note that the (100)1 × 1 phase has not been detected for MnO on Ag(100) in the 2-D monolayer limit. The MnO(100)1 × 1 phase is observed in the form of 3-D islands [20–22], but for the monolayer only a (2 × 1) structure has been observed for MnO on Ag(100) [20], as discussed below. Presumably, the higher strain as a result of the larger lattice mismatch of MnO precludes the formation of a (100)1 × 1 wetting layer on Ag(100).

A more complex structure system, which may be traced back to the RS (100)-type motif, is the c(4 × 2) structure observed for several TM oxides on Pd(100). The c(4 × 2) structure has been reported for NiO_x [23, 24], CoO_x [25] and MnO_x [26], and is theoretically predicted for FeO_x [27], and it thus seems to constitute a more general 2-D structure concept. Figure 1.4 illustrates the structural ingredients of the c(4 × 2) phase for the example of CoO_x on Pd(100) [28]. The STM image of Fig. 1.4a shows the c(4 × 2) periodicity with respect to the Pd(100) surface, where the c(4 × 2) and the primitive rhombic unit cells are indicated and labeled A and B. Two types of defects are visible on the image with darker and brighter contrast, presumably due to missing cations and adsorbate species, respectively. The LEED pattern in Fig. 1.4b with sharp spots confirms that the surface is well ordered, the c(4 × 2) (A) and the primitive (B) unit cells are also drawn. The high-resolution STM image (Fig. 1.4c) reveals that the structure is characterized by large bright maxima defining the c(4 × 2) unit cell and smaller and less-bright protrusions in a zig-zag line following the ⟨011⟩ Pd substrate directions. Alternatively, the c(4 × 2) unit cell may also be spanned by the dark depressions in between the bright spots.

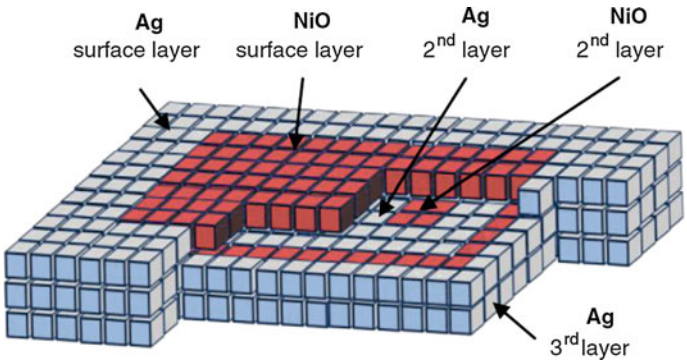

Fig. 1.3 Schematic model of a NiO(100)1 × 1 island embedded in Ag(100); *blue* Ag atoms; *red* NiO. Reproduced with permission from [19] (Color figure online)

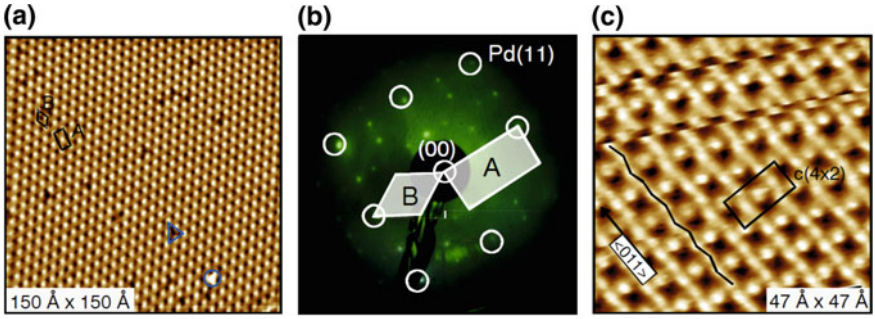

Fig. 1.4 CoO_x/Pd(100) c(4 × 2) phase: **a** STM image (15 × 15 nm^2); V_S = +1 V; I_T = 0.1 nA. **b** LEED pattern (electron energy 104 eV). **c** Atomically resolved STM image (4.7 × 4.7 nm^2); V_S = +0.08 V; I_T = 0.1 nA). The characteristic features, i.e. the rectangular c(4 × 2) unit cell and the zig-zag chain of atoms, are highlighted. Reproduced with permission from [28]

According to the DFT calculations, the Co atoms are imaged as maxima in the STM, whereas the O atoms are imaged dark [25].

The c(4 × 2) structure may be modeled by a RS (100) plane, into which 1/4 of cation vacancies has been introduced, defining the c(4 × 2) unit cell and a formal M_3O_4 stoichiometry. This is shown for Mn_3O_4 supported on Pd(100) in Fig. 1.5: the square RS (100)-type lattice is given by the Mn atoms (light gray) and O atoms (red), the circles denote the Mn vacancies, the dashed lines trace the 2-D unit cell, and the solid zig-zag line indicates the Mn lateral displacements in the relaxed structure model [29], as discussed below. Franchini et al. [26, 29] have investigated the Mn_3O_4 c(4 × 2) structure in detail with standard and generalized DFT, considering different adsorbate registries to the Pd substrate as well as different magnetic ordering models. The most stable adsorbate configuration was generally found with the Mn atoms located above the Pd hollow sites and the O atoms on top of Pd

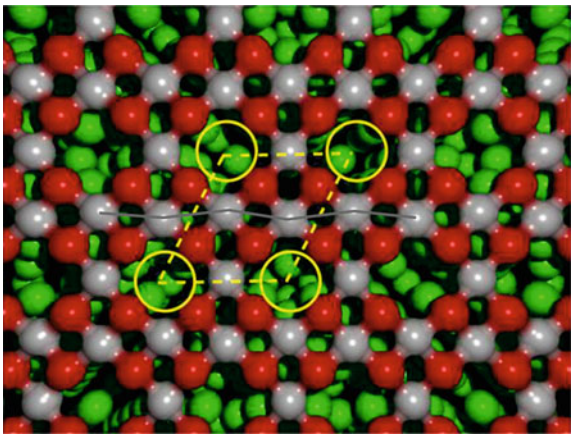

Fig. 1.5 Top view of the geometrical model of the c (4 × 2) Mn_3O_4 phase on Pd (100) (*red* O atoms; light *grey* Mn atoms; *small green spheres* Pd atoms underneath). *Dashed lines* indicate the 2-D unit cell, full line the Mn lateral displacements, *circles* highlight the position of vacancies. Adapted from [29]

surface atoms (RH1 model), but depending on the choice of the functionals in the calculations antiferromagnetic (AFM2) or ferromagnetic (FM) order was predicted as the lowest energy ground state. However, using the HSE hybrid functional approach a slight preference for the FM configuration as the thermodynamic ground state was obtained [26]. In order to validate this result, experimentally accessible quantities, namely STM images and phonon frequencies, have been simulated for the RH1-AFM2 and RH1-FM models and compared to the measured values. Figure 1.6 shows the optimized geometrical structure for the RH1-FM and RH1-AFM2 magnetic configurations. In both models, there is a significant in-plane lattice distortion with large lateral displacements of Mn and O species, particularly around the Mn vacancies. These distortions are a means to relax the interfacial strain in the overlayer and are reminiscent of a 2-D polaronic distortion. However, whereas the RH1-FM model leads to a flat surface, the RH1-AFM2 model gives a vertical bucking between the oxygen atoms. These geometrical differences are, however, difficult to evaluate in the experimental STM images. There are two types of Mn atoms in the structure, which may be loosely associated with Mn^{2+} and Mn^{3+} species, which have different densities of states (DOS) and magnetic moments and, significantly, which are distinctly different for the two magnetic structure models. The DOS are reflected in the STM contrast and thus allow us to distinguish between

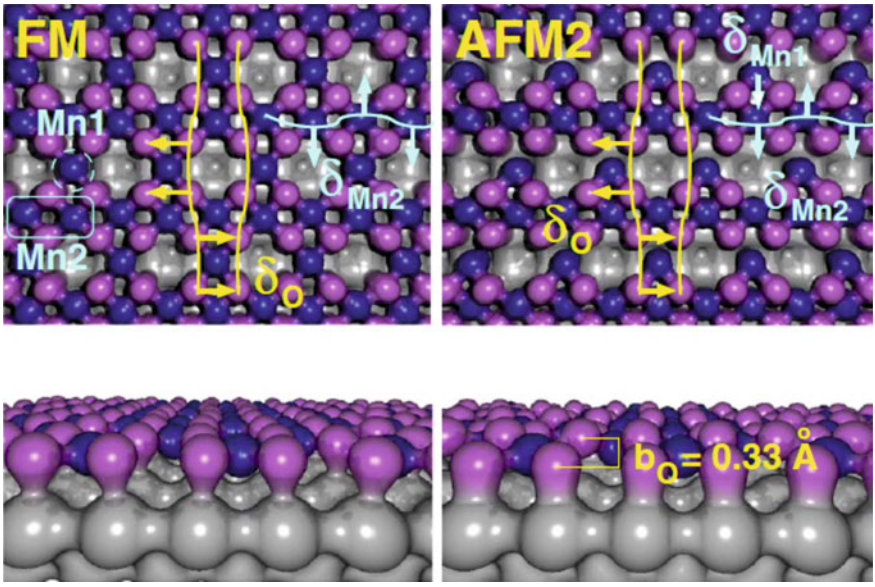

Fig. 1.6 Optimized geometrical structure for the c(4 × 2) Mn_3O_4 RH1 model in FM (*left*) and AFM2 (*right*) magnetic configuration (*light grey* Pd substrate atoms; *pink* O atoms; *blue* Mn atoms). Two distinct Mn species are distinguishable: Mn1 sandwiched between two vacancies and two Mn2 atoms, forming the *zig-zag lines* as highlighted. Strain is indicated by the *arrows*. Note the vertical buckling b_O between oxygen atoms in the AFM2 model. Reproduced with permission from [26]

the models: it turns out that only the RH1-FM model gives the correct contrast in the STM simulations, which is compatible with the experimental image (see Fig. 1.7).

The phonon structure is a highly diagnostic means in the analysis of complex oxide phases [5]. HREELS experiments have established that the phonon loss spectrum of the Mn_3O_4 c(4 × 2) surface has a single pronounced peak at 44 meV [29]. The DFT calculations for the FM structure found a single dipole active phonon mode in perfect agreement with this experimental value. This phonon mode results from the antiphase and out-of-plane vibrations of the O and Mn sublattices perpendicular to the surface, a mode that is typical of the ideal MnO(100) surface, thus giving overall credence to the (100)-type derived structure model of the c(4 × 2) structure.

The STM and phonon measurements in conjunction with the DFT calculations support a ferromagnetic model as the lowest energy ground state of the c(4 × 2) structure. However, an independent experimental confirmation would still be desirable. Altieri et al. have performed X-ray magnetic circular dichroism (XMCD) experiments of the Mn_3O_4 c(4 × 2) phase [30]. The experiments have been carried out on a c(4 × 2) Mn_3O_4 phase on a stepped Pd(1 1 21) surface, a vicinal to Pd (100), because the overlayer can be prepared in a virtually defect-free single domain structure on this surface (see Sect. 1.4). A clear magnetic anisotropy in the temperature and field dependent Mn $L_{2,3}$ XMCD spectra has been detected, but the sample remained paramagnetic down to 8K, the lowest temperature attainable in the experiments. Thus, a ferromagnetic state could not be confirmed, perhaps the temperature in the experiment was still too high. The observed magnetic anisotropy with its easy axis perpendicular to the surface has been related to a largely unquenched orbital moment as revealed by XMCD sum rule analysis [30]. A model considering the effects of the crystal field acting on the Mn cations in the c(4 × 2) Mn_3O_4 structure, where the Mn vacancies hole dope the 3d states, has been

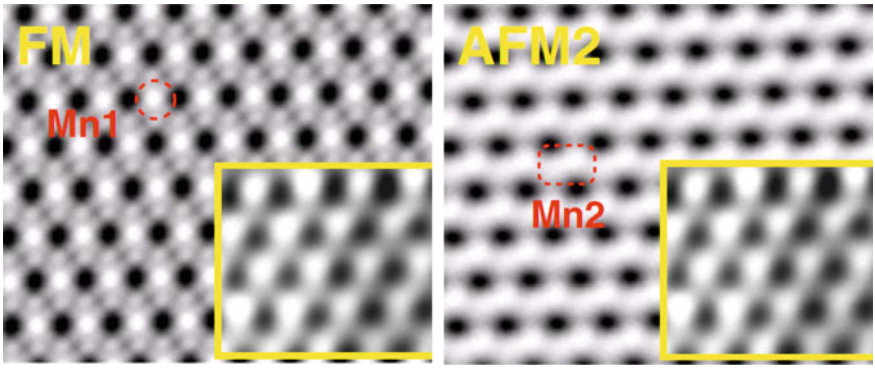

Fig. 1.7 Simulated STM images of the RH1-FM and RH1-AFM c(4 × 2) Mn_3O_4 structures compared with the experimental STM image (reproduced in the *inserts*). Mn atoms appear as bight maxima, the O atoms are not seen. Reproduced with permission from [26]

proposed to account for this perpendicular magnetic anisotropy. This is in accord with the proposed geometry and structure model of the c(4 × 2) phase. Although the problem of ferromagnetism in c(4 × 2) Mn_3O_4 remains an open question, the XMCD measurements of Altieri et al. have demonstrated that 2-D oxide systems may indeed support interesting magnetic behavior.

Hexagonal monolayer structures. A hexagonal oxide monolayer can be realized within the planar BN structure, if boron and nitrogen are replaced by metal and oxygen species. Goniakowski and Noguera have derived this structure (they called it graphite-like B_k structure) from theoretical considerations of polarity compensation for the MgO(111) monolayer on Ag(111) [31], and their model is consistent with the experimental observations of MgO(111) thin films on Ag(111) by Kiguchi et al. [32] (see also Chap. 7 by Noguera and Goniakowski). For ZnO monolayers on Ag(111), Tusche et al. [33] have proposed the hexagonal BN-type structure on the basis of surface X-ray diffraction and STM results, emphasizing the depolarization character of this structure, which is accompanied by a significant lateral expansion of the lattice constant and a reduced Zn–O bond length within the ZnO sheets. For film thicknesses exceeding 3–4 ML, a transition to the bulk wurtzite structure has been observed [33]. The hexagonal planar structure has also been reported for ZnO on Pd(111) [34]. A (6 × 6) structure has been detected in the STM and LEED experiments, which has been rationalized by DFT calculations in terms of a Zn_6O_6 coincidence structure of the BN-type. This structure is thermodynamically the most stable phase over a large range of oxygen chemical potentials for the monolayer and for coverages up to 4 ML, but converges to the bulk wurtzite structure for thicker films [34].

Uniaxial monolayer structures. The (2 × 1) structures reported for NiO and MnO on Ag(100) at the monolayer stages of growth fit into this category [18, 20]. Figure 1.8 shows STM images of the MnO(2 × 1) phase on Ag(100) [20]: the oxide grows in elongated stripes along the high symmetry ⟨110⟩ directions of the substrate (Fig. 1.8a), with bright and dark lines separated by twice the Ag lattice constant, which define the ×2 order parameter. The peculiar growth pattern in form

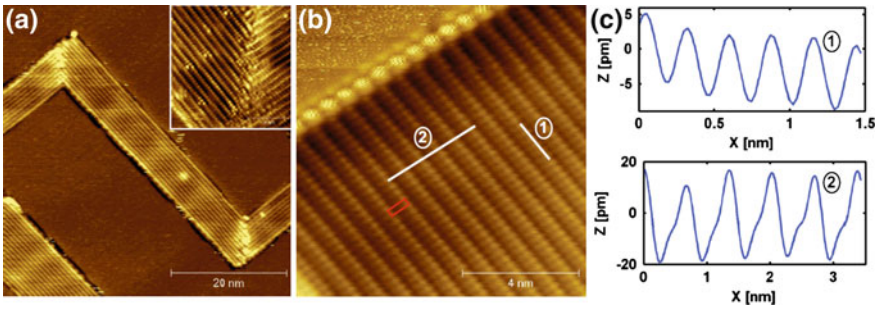

Fig. 1.8 High-resolution STM images of the MnO(2 × 1) structure on Ag(100): **a** $V_S = -1.9$ V; $I_T = 0.1$ nA; **b** $V_S = -1.0$ V; $I_T = 0.1$ nA. The *insert* in (**a**) shows a domain boundary between two orthogonal (2 × 1) stripes. **c** Line scans along the lines 1 and 2 of image (**b**). Adapted from [20]

of narrow oxide stripes is due to a symmetry breaking kinetic growth phenomenon, which has been ascribed to the asymmetric attachment and diffusion energies of ad-atoms at the (2 × 1) island boundaries [20]. The high-resolution STM image of the (2 × 1) structure in Fig. 1.8b reveals the atomic maxima along the bright lines and at the upper left hand corner a MnO–Ag island edge, which is decorated by bright blobs due to an electronic contrast phenomenon at the island boundary. The STM line scans in Fig. 1.8c, following the lines indicated in (b), give measured corrugations of ∼10 and ∼40 pm along and across the (2 × 1) lines, respectively. The DFT calculated model of the MnO(2 × 1) structure on Ag(100) is depicted in Fig. 1.9a. The Mn atoms (blue) are distinguished by threefold oxygen (red) coordination or, alternatively, O–Mn–O zig-zag lines; the condensation of either of these structure elements into a 2-D structure and superimposing it onto the square Ag substrate yields a quasi-hexagonal network with alternating Mn–O up and down zig-zag rows. These rows form the ×1 lines of the (2 × 1) structure, whereby the protruding O atoms are imaged bright in the STM, as shown by the simulated STM image in Fig. 1.9a, left panel. The (2 × 1) structure is polar and its total energy as calculated by DFT is only at a local minimum: it is thus a meta-stable phase, with

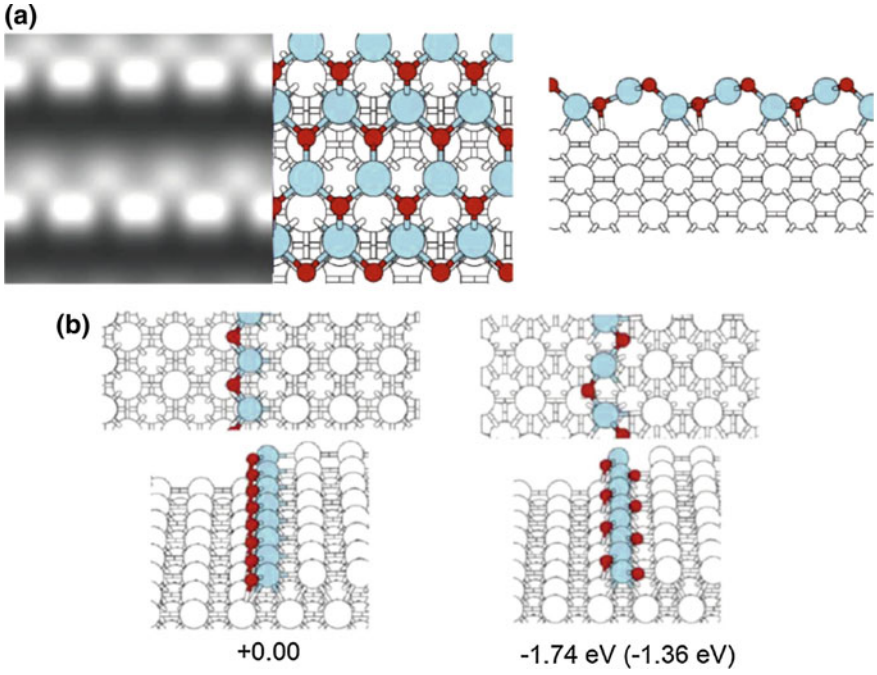

Fig. 1.9 **a** Structural model (*top* and *side views*) and simulated STM image at a bias +1.0 V of the (2 × 1) phase of MnO on Ag(100) (*blue* Mn atoms; *red* O atoms). **b** Growth of a MnO stripe on the border of a step on Ag(100): the structure and energetics of the (100)1 × 1-like stripe (*left*) against the (2 × 1)-like stripe (*right*) are compared, as derived from a DFT + U approach (U = 4.5 eV) or B3PW91 (*in parenthesis*). Adapted from [20] (Color figure online)

the MnO(100)1 × 1 phase being the thermodynamically stable ground state. The (2 × 1) phase, which in the case of MnO/Ag(100) is the predominant phase observed experimentally for the monolayer, must therefore be kinetically stabilized during growth. Obermüller et al. [20] have investigated theoretically the stability of MnO line elements at Ag step edges (see also Chap. 2 by Fortunelli et al.). Figure 1.9b shows (1 × 1)-type (left) and (2 × 1)-type (right) MnO stripes at the border of a silver step on Ag(100), comparing their relative stabilities: the (2 × 1)-like pattern is more stable than the (1 × 1)-like pattern, by a significant amount of >1.30 eV per MnO unit, mainly due to the cancelation of polarity. The kinetic nucleation of the (2 × 1) structure motif at Ag step edges is thus favorable, and once nucleated, the (2 × 1) structure continues to grow into the two-dimensional layer.

The (6 × 1) NiO structure on Rh(111)-type surfaces [35, 36] illustrates the formation of a uniaxial structure via the incorporation of Ni–O coordination spheres of different symmetry, namely triangular threefold coordinated and quadratic fourfold coordinated oxygen units. Both structure elements are related to the RS (100) and RS (111) surface orientations. The combination of these structure units leads to the development of troughs and ridges along the [110] surface direction. Figure 1.10 displays a high-resolution STM image of the (6 × 1) structure (upper part) and the DFT derived structure model (lower part); the triangular and quadratic oxygen units are colored dark and bright red, respectively [36]. The structure may be viewed as containing Ni–O sheets with quadratic O coordination, which are connected via Ni atoms contributing to the triangular O coordination units: this leads to a complex line pattern in STM (see Fig. 1.10), which however has been reproduced rather well in the DFT simulations [36]. The calculations of the phase stability diagram for monolayer-thick NiO layers on Rh(111) demonstrated that

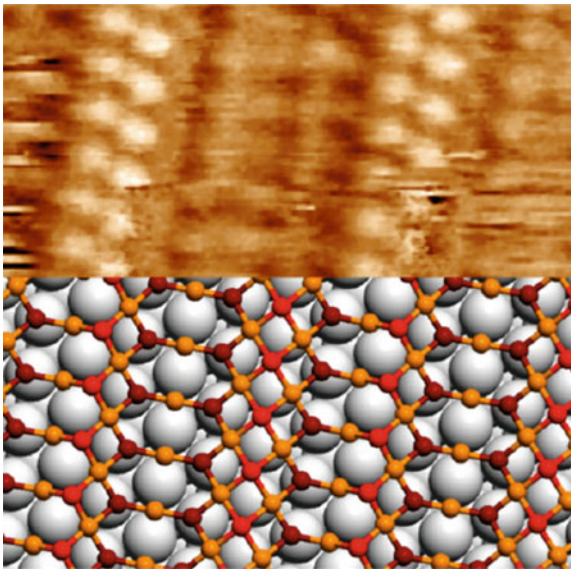

Fig. 1.10 STM image and corresponding model of the NiO(6 × 1) structure on Rh (111). Adapted from [36]

within the range of experimentally accessible oxygen potentials the (6 × 1) with a Ni_5O_5 stoichiometry is the most stable phase. Another example of a uniaxial surface oxide has been reported for NiO on Pt(111) by Hagenbach et al. [37], where a (7 × 1) structure with a pattern of bright lines in the STM has been observed. The tentative structure model of Hagenbach et al. employed again a combination of square and triangular Ni–O units [37].

1.2.2 Oxide Bilayer and Trilayer Structures

Hexagonal oxide bilayers. Hexagonal oxide bilayer structures may be derived from three structure motifs: (i) a stacking of densely packed hexagonal planes of cations and anions, as in the RS (111)-type stacking sequence (Fig. 1.11a); (ii) a honeycomb lattice of hexagons sharing sides (Fig. 1.11b); and (iii) a kagomé lattice, containing hexagons that are interconnected through their vertices and create triangles defined by the connection points (Fig. 1.11c). While the latter two lattices have been encountered only on hexagonal substrate surfaces, e.g. fcc (111)-type metal surfaces, the first structure has been reported on both hexagonal (111) and square (100) substrates.

The FeO(111) wetting layer on Pt(111) is a benchmark system of the *RS (111)-type bilayer* structure on a hexagonal substrate surface [38–43]. This bilayer is composed of the close packed oxygen layer forming the outer surface and the Fe layer at the Pt interface. As a result of the significant lattice mismatch, the overlayer is almost incommensurate and displays a characteristic Moiré modulation in the STM images [38, 39, 41, 42]; in fact, up to four different high-order coincidence structures and concomitant Moiré patterns have been reported, depending on the exact FeO coverage [41]. The FeO bilayer cannot grow much beyond two monolayers and, for higher coverages, is transformed into a $Fe_3O_4(111)$ island phase [41]. This is due to the polar character of the FeO bilayer, which precludes further 3-D growth. The Fe–O interlayer distance of the bilayer has been measured by X-ray photoelectron diffraction by Kim et al. [40] and a compression of about 50 % relative to bulk FeO has been detected. This interlayer contraction is a way to

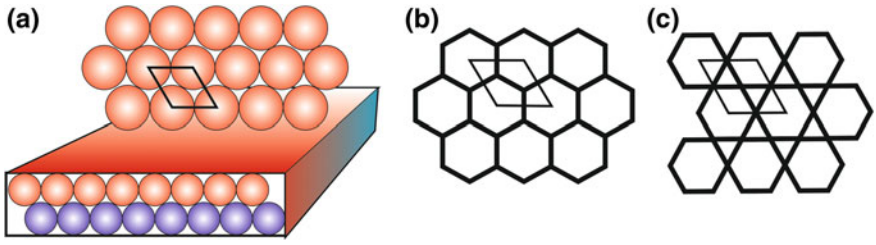

Fig. 1.11 Schematic drawings of: **a** hexagonal RS (111)-type bilayer; **b** honeycomb lattice; **c** Kagomé lattice

reduce the surface dipole and the electrostatic energy and thus adds to the stability of the bilayer. The screening of the FeO surface dipoles by the proximity of the Pt substrate is another mechanism to reduce the polarity in this 2-D system. A very similar FeO(111) bilayer geometry as for FeO/Pt(111) has been reported recently also on a Pd(111) substrate [44], with very similar STM fingerprints; it appears that the chemical nature of the substrate has only a minor influence on the details of the FeO(111) overlayer structure.

Whereas the growth of a hexagonal oxide bilayer on a hexagonal substrate is intuitively persuasive, it is more interesting on a square (100) substrate. The FeO c(2 × 10) on Pt(100) [45] and c(8 × 2) on Pd(100) [46] phases, the CoO c(10 × 2) phase on Ir(100) [47], or the CoO (9 × 2) phase on Pd(100) [48] can be interpreted in terms of a RS (111)-type structure. Here, the CoO (9 × 2) structure on Pd(100) is discussed as a prototypical example [28, 48]. Figure 1.12 displays STM images of the CoO (9 × 2) coincidence structure at different magnifications [28]. The structure is characterized by lines of elongated rod-like maxima along the substrate [0–11] direction (Fig. 1.12a, b—dashed line in b), which can be resolved into atomic protrusions along the orthogonal [011] direction at higher magnification (Fig. 1.12c). These [011] lines of maxima are laterally undulated (indicated by the thin solid line in panel c) and show a significant contrast modulation with four brighter and four darker maxima; the latter is also recognized in the self-correlation plot of the STM image (d). The CoO (9 × 2) structure has been modeled in DFT by a (111)-type bilayer as shown in Fig. 1.13, with the O plane at the surface and the Co plane at the Pd interface [48]. In the relaxed geometry, the bilayer becomes significantly distorted, with strong height modulations in both Co and O sublattices, which tend to interpenetrate each other to reduce the polarity of the bilayer and the interfacial strain. These height modulations are reflected in the atomic contrast modulations seen in the STM image (Fig. 1.12c), which have been reproduced well by the respective DFT simulations [48].

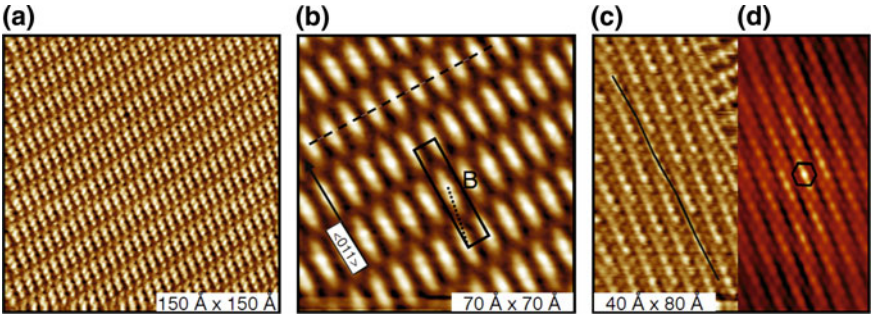

Fig. 1.12 **a–c** STM images of the CoO (9 × 2) coincidence phase on Pd(100) (**a** (15 × 15 nm^2); V_S = +0.01 V; I_T = 1.0 nA. **b** (7 × 7 nm^2); V_S = +1.0 V; I_T = 0.1 nA. **c** (4 × 8 nm^2); V_S = +0.01 V; I_T = 1.0 nA). The *rectangular* (9 × 2) unit cell of the coincidence mesh is indicated in (**b**). **d** Self-correlation image of the STM image of panel (**c**); here the *quasi-hexagonal* cell of the CoO lattice is highlighted. Reproduced with permission from [28]

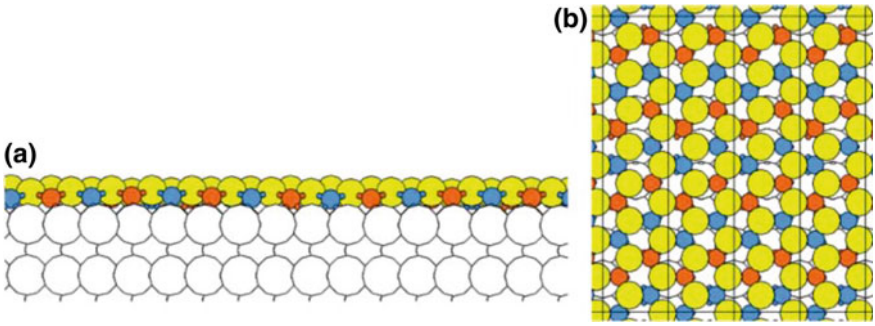

Fig. 1.13 **a** Side view of the (9 × 2) bilayer structure showing the Pd–Co–O stacking. **b** Top view of four unit cells of the (9 × 2) structure. Pd atoms are depicted in *white*, O atoms in *yellow* and Co atoms in *blue* and *red*, reflecting the AFM3 magnetic ordering of the CoO layer. Reproduced with permission from [48]

The CoO (9 × 2) phase has been found in the experiments to coexist frequently with the Co_3O_4 c(4 × 2) structure at the same Pd surface. This is in agreement with the DFT calculations, which predict a similar thermodynamic stability of the two phases, with only a slight preference for the (9 × 2) [48]. The STM images of Fig. 1.14 show an interesting aspect of the coexisting (9 × 2) (left) and c(4 × 2) (right) Co-oxide monolayer phases: the two phases are separated by a well-defined 1-D interface boundary, with a smooth transition from one structure into the other. In the c(4 × 2) structure of Fig. 1.14a (right), the dark depressions form the primitive unit cell and are due to the Co cation vacancy holes of this structure (see

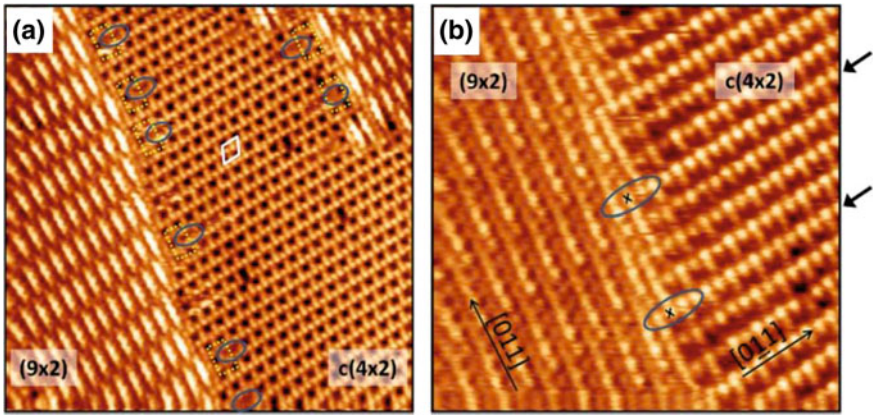

Fig. 1.14 STM images of the Co oxide (9 × 2) (*left*) and c(4 × 2) (*right*) monolayer structures coexisting on Pd(100), displaying a smooth 1-D interface. **a** [(15 × 15 nm^2); V_S = +0.08 V; I_T = 0.6 nA]. The *ellipses* at the c(4 × 2) side of the interface indicate regions with a modified arrangement of dark vacancies. **b** [(8 × 8 nm^2); V_S = +0.01 V; I_T = 1.0 nA]. The *crosses* inside the ellipses at the interface mark bright protrusions apparently belonging to both (9 × 2) and c(4 × 2) structures. Reproduced with permission from [48]

Sect. 1.2.1). Close to the (9 × 2) boundary, the pattern of dark depressions is altered as highlighted by the elipses in the figure, shifting from rhombic to square. Although the exact atomic structure of the region at the c(4 × 2)/(9 × 2) interface cannot be recognized, it has been speculated that additional Co species may have been introduced, leading to a local reduction of the Co_3O_4 c(4 × 2) stoichiometry towards the CoO (9 × 2) stoichiometry and contributing to the smooth boundary. This has been confirmed by the DFT calculations [48].

Moreover, at this point it is worth addressing an interesting technical problem. The interpretation of STM images of oxide materials relies on the identification and assignment of contrast features to atomic species. The oxide community has learnt that this requires, apart from the most simple systems, the help of theoretical simulations. In the case of the c(4 × 2) M_3O_4 phases, it has been generally accepted that the M cations are imaged as bright protrusions [25, 26, 29, 48]. At the (9 × 2)/c(4 × 2) 1-D interface in Fig. 1.14b, there are bright features marked by crosses, which are a continuation of the c(4 × 2) lines but apparently also belong to the (9 × 2) structure. This would suggest that the bright STM protrusions of the (9 × 2) structure can be identified also with Co species, as in the c(4 × 2) structure. This, however, is difficult to reconcile with the bilayer structure model. Gragnaniello et al. [48] have gone into an extensive DFT study of the problem, and found that, while indeed the Co species are imaged bright in the c(4 × 2) structure, the bright maxima in the (9 × 2) structure are located at the oxygen sites: this is the result of the complex interaction of electronic and geometrical degrees of freedom contributing to the STM contrast in this strongly distorted bilayer oxide. The simulations of the 1-D interface revealed that the bright protrusions highlighted by the crosses in Fig. 1.14b are identified as bright oxygen protrusions, thus providing a consistent picture of the interface and of the structural assignment of both 2-D Co oxide phases [48].

The first layer of vanadium oxide on Pd(111) displays a *hexagonal honeycomb lattice*, as recognised from the STM image of Fig. 1.15a. This V surface oxide has

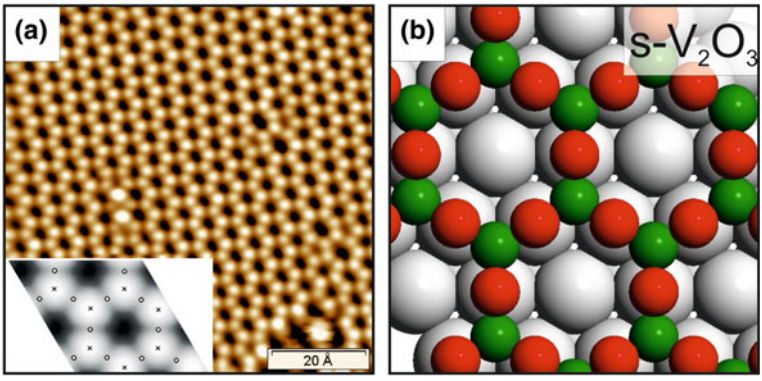

Fig. 1.15 STM image of the honeycomb surface-V_2O_3 (2 × 2) phase on Pd(111) (**a**) and respective DFT model (**b**) (*green* V; *red* O; *grey* Pd). The *insert* in (**a**) displays the DFT simulated STM contrast. Adapted from [54]

been grown under moderately oxidizing conditions [49], it forms a simple (2 × 2) superstructure and has been interpreted in terms of a bilayer with V_2O_3 stoichiometry [50, 51]. According to the DFT analysis, the V atoms are situated in three-fold hollow Pd sites and the O atoms are on-top of Pd surface sites (see the model in Fig. 1.15b), with the O layer ∼0.7 Å outside the V plane [51, 52]. This *surface*-V_2O_3 phase is polar and cannot grow beyond the first layer. With increasing oxide coverage, a sequence of other complex phases has been observed [50, 53], until the oxide overlayer converges to the bulk V_2O_3 phase, which is the stable compound under the thermodynamic conditions of typical surface science growth experiments. It has to be stressed that the surface *s*-V_2O_3 honeycomb geometry is a particular 2-D phenomenon and not a structure element of the V_2O_3 bulk corundum structure.

The Ti_2O_3 bilayer on Pt(111) [55, 56] is related to the *surface*-V_2O_3 phase on Pd (111), but it features an interesting structural difference: it forms a *kagomé lattice*, which can be discerned in the experimental STM image of Fig. 1.16a and the respective STM simulation (Fig. 1.16b). The kagomé lattice with a lattice constant of ∼6 Å, as derived from LEED and STM measurements, is incommensurate with the Pt lattice; overall it is less dense than a corresponding honeycomb lattice. It could be speculated that the reason for the Ti_2O_3 forming the kagomé lattice on Pt (111) may be due to the poor fit of Ti–O bond distances onto the Pt lattice, the result of which is a less dense incommensurate structure. In the case of V_2O_3 on Pd(111), the V–O bonds fit exactly onto the (2 × 2) structure formed by the denser honeycomb lattice. Finally, it is noted that the $(\sqrt{7} \times \sqrt{7})R19.1°$ vanadium oxide layer on Rh(111), which can been grown under highly oxidizing conditions, displays also a kagomé lattice pattern—see Fig. 1.18a. However, this phase with a formal V_3O_9 stoichiometry is not strictly a bilayer structure but more complex, and is better discussed in terms of a local building block picture in Sect. 1.2.3.

Hexagonal oxide trilayers. A hexagonal O–M–O trilayer slab may be cut out of the RS structure perpendicular to the [111] direction. The slab is apolar and stable from the electrostatic point of view and corresponds formally to a MO_2

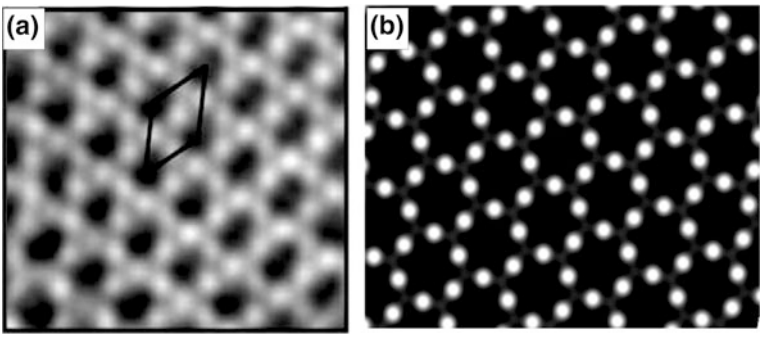

Fig. 1.16 STM image of the Ti_2O_3 kagomé phase on Pt(111) (**a** (3 × 3 nm^2); V_S = −0.4 V; I_T = 1.06 nA) and theoretically simulated STM image at V = −0.4 V (**b**). Adapted from [56]

stoichiometry. The oxygen layer at the interface is however shared with the metallic substrate and the real oxidation state is thus somewhat lower, e.g. $MO_{2-\delta}$. Hexagonal trilayer structures have been proposed for the intrinsic surface oxides of some group VIII metals such as Ru [57] or Rh [58]. The hexagonal $VO_{2-\delta}$-hex phase on Pd(111) [50], the hex-$MnO_{2-\delta}$ phases on Pd(100) [29], the hex-CoO_x phase on Pd(100) [28], and the c(8 × 2) $CoO_{2-\delta}$ structure on Ir(100) [59] have also been interpreted within this trilayer structure concept. Apart from the last $CoO_{-\delta}$/Ir system, the other hetero-trilayers form incommensurate overlayers. An interesting case is the $FeO_{2-\delta}$ trilayer on Pt(111). It has been observed after oxidation of the FeO(111) bilayer at high oxygen pressures [60]. This trilayer phase is of catalytic relevance, since it has been shown to be the active surface in the low temperature oxidation of CO [61, 62]. Recently, Zeuthen et al. [44] have presented an STM view of an intermediate stage of the oxidation, performed with atomic oxygen, of the FeO(111) bilayer on Pd (111). We recall that the FeO(111) bilayer on Pd(111) is isostructural with the one on Pt(111). Figure 1.17a, b displays STM images, in which O–Fe–O islands (bright contrast) coexist with O-adatom line dislocations, the latter are formed during the initial stages of the oxidation. Panel (c) gives a schematic picture of the structural changes during the bilayer-trilayer transformation [44].

Hexagonal trilayers of 2-D oxides may also be derived from the fluorite structure in [111] direction: this is the case for ceria monolayers on metal surfaces, where generally ceria (111)-type O–Ce–O hexagonal structures have been reported [63–67]. However, the CeO_2 (111) surface is the most stable surface termination of bulk CeO_2, and the occurrence of related structures in monolayer systems does not require the presence of low-dimensional effects for their stabilization.

1.2.3 Complex Binary Oxide Structures

As mentioned above, the term “complex” is used here to indicate that the structures under consideration contain various structure elements of different symmetry, a combination of different M–O building blocks, or different oxidation states. The TM elements at the left of the Periodic Table, such as Ti, V, or W provide flexible oxidation states and a variety of M–O coordination spheres that can support several oxides of this category. The phase diagram of 2-D V-oxides on Pd and Rh surfaces is particularly rich in such complex structure systems, as discussed below.

Figure 1.18a shows an STM image of the $(\sqrt{7} \times \sqrt{7})$R19.1° structure of V-oxide on Rh(111), a phase that can be fabricated under highly oxidizing growth conditions. The pattern corresponds to a hexagonal kagomé lattice, but simple models failed to account for the experimental facts. The structure was difficult to analyze, but eventually has been resolved by a combination of electronic and vibrational energy level spectroscopies and extensive DFT modeling [68]. Accordingly, the structure is composed of quadratic pyramidal VO_5 building blocks, which have four oxygen atoms in the basal plane attached to the substrate, the V atom in the center and a vanadyl V = O group at the apex (see Fig. 1.18c). These VO_5 units are joined

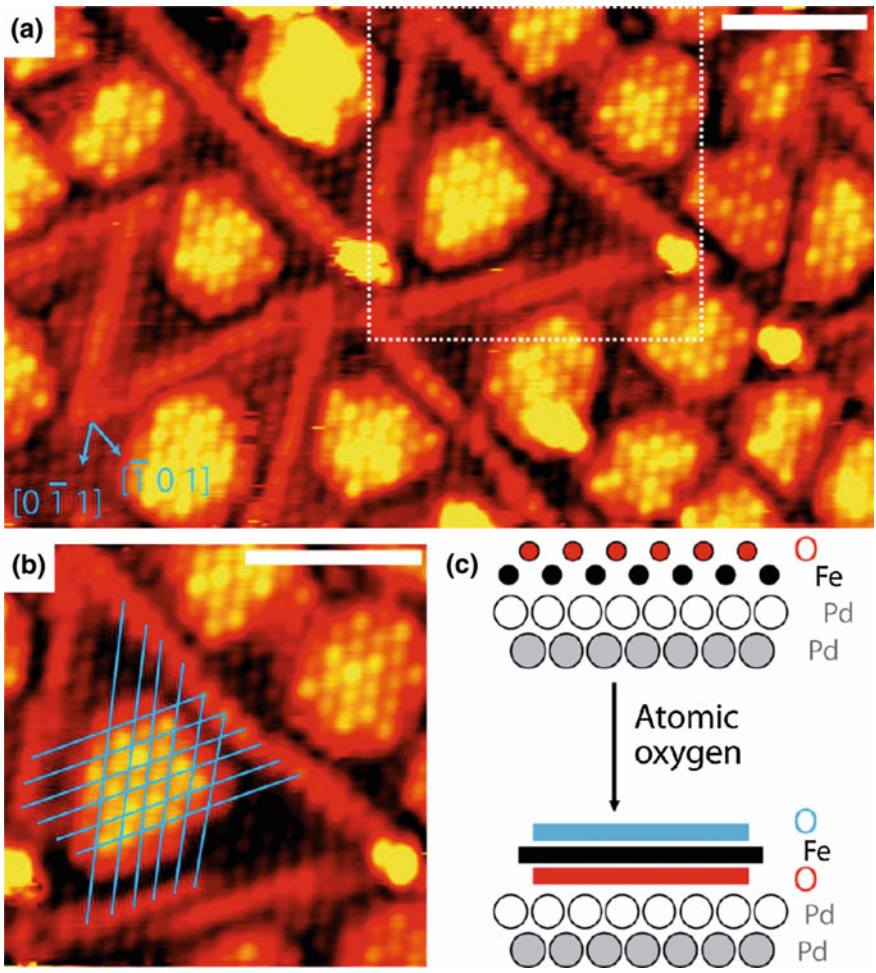

Fig. 1.17 **a**, **b** STM images (scale bars are 2.5 nm; $V_S = 0.30$ mV; $I_T = 229$ nA) showing O–Fe–O trilayer islands coexisting with O-adatom dislocations. Images were obtained after 300 s of O exposure at $p(O_2) = 1 \times 10^{-7}$ mbar at 300 K. **b** Enlargement of the area indicated by the *dotted square* in (**a**). Guidelines mark the Fe positions of the pristine FeO film that coincide with the protrusions on the O–Fe–O islands. **c** Proposed structural changes upon formation of O–Fe–O trilayer islands. Reproduced with permission from [44]

together in a corner sharing way to generate the $\sqrt{7}$ unit cell as indicated in Fig. 1.18b. This model has been substantiated by the very characteristic phonon frequency of the V = O group in the high-resolution electron energy loss (HREELS) spectra [68]. The formal stoichiometry according to this model corresponds to V_3O_9 or VO_3, which would violate the maximum possible oxidation state of V atoms of +5. Therefore, the structure requires charge transfer from the Rh(111) substrate to the oxide layer to enable its stability. An intriguing feature of the $(\sqrt{7} \times \sqrt{7})$R19.1°

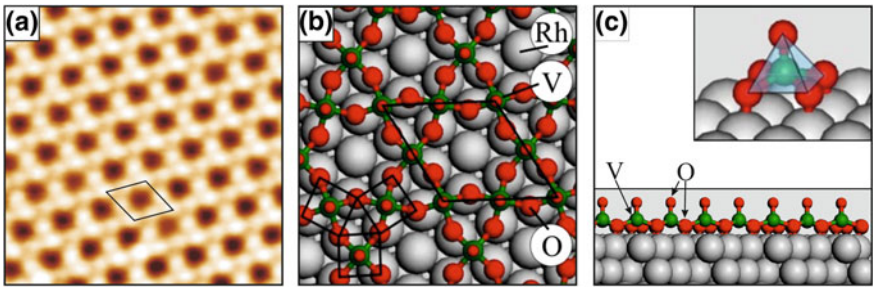

Fig. 1.18 **a** High-resolution STM image of the ($\sqrt{7} \times \sqrt{7}$)R19.1° V_3O_9 phase on Rh(111) (5×5 nm^2); **b** DFT structure model, *top view* (*green* V; *red* O; *grey* Rh). **c** Structure model, *side view*; the *insert* shows a detailed view of the pyramidal O_4V = O units. Adapted from [70, 71]

V_3O_9 model is that its VO_5 building blocks can also explain the formation of the ($\sqrt{13} \times \sqrt{13}$)R13.8° V-oxide structure, which has been frequently found in coexistence with the ($\sqrt{7} \times \sqrt{7}$)R19.1° phase at the same surface. A simple rearrangement of the VO_5 pyramids can generate a ($\sqrt{13} \times \sqrt{13}$)R13.8° unit cell with a V_6O_{18} content, which breaks down again to the formal VO_3 stoichiometry [68]. The formation of such highly oxidized V-oxide phases is not restricted to the Rh substrate, but has also been observed on Pd(111), where a (4×4)-V_5O_{14} monolayer phase has been detected [53, 54, 69]. The V_5O_{14} layer is oxygen terminated on both sides and forms an open hexagonal network with V atoms in an unusual tetrahedral O coordination, which interacts with the Pd surface alternately with one or two oxygen atoms of the VO_4 tetrahedra [54]. Again, charge transfer from the metal across the interface to the oxide via the anchoring O atoms is necessary to stabilize this structure. The highly oxidized V-oxide phases on Rh(111) and Pd(111) provide prototypical examples of how the electronic metal-oxide interface coupling enables unusual oxidation states and new structure concepts in 2-D oxide systems.

The ($\sqrt{7} \times \sqrt{7}$)R19.1° V_3O_9 phase on Rh(111) can be reduced to a ($5 \times 3\sqrt{3}$)-rect structure [72]. Figure 1.19a shows a larger scale STM image of islands of this rectangular structure, for sub-monolayer coverage, and the insert presents a high-resolution STM image displaying an intriguing pattern. The DFT derived structure model, given in Fig. 1.19b, contains two major structure elements: the highly oxidized quadratic VO_5 pyramids introduced above, and more reduced hexagonal V_6O_6 ring structures, joined together in a complicated way to generate the ($5 \times 3\sqrt{3}$)-rect unit cell, with a $V_{13}O_{21}$ stoichiometry content. The STM image calculated from this model in the insert of Fig. 1.19b reproduces in detail all the features of the experimental image contrast in Fig. 1.19(a—insert), and thus gives credence to this complex structure model. Further reduction of the ($5 \times 3\sqrt{3}$)-rect leads to a (9×9) structure, in which all the VO_5 units are reduced and the structure is formed by a complicated network of V_6O_6 hexagons [72]. The overall stoichiometry of this (9×9) phase on Rh(111) is reduced to V_2O_3.

From the phase diagram of Ti-oxides on Pt(111), which contains a number of reduced phases [56], the so called zig-zag-like phase is selected here for the

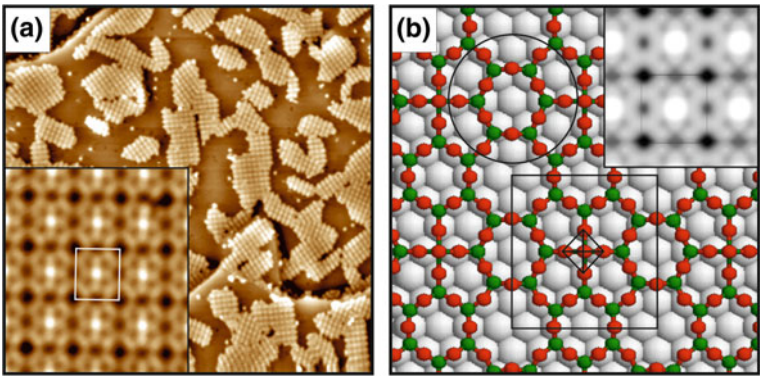

Fig. 1.19 **a** STM images of the (5 × 3√3)-rect V-oxide phase on Rh(111) (main frame: (100 × 100 nm^2); V_S = +2.0 V; I_T = 0.1 nA; *insert* (3.3 × 3.3 nm^2); V_S = +2.0 V; I_T = 0.1 nA). **b** DFT model of the (5 × 3√3)-rect $V_{13}O_{21}$ phase (*green* V; *red* O). The *insert* shows a DFT simulated STM image. Adapted from [71]

discussion [73]. The zig-zag phase (see STM image of Fig. 1.20a) is formed by three-atom wide stripes separated by dark troughs running along the ⟨1−10⟩ substrate directions and with a zigzag pattern of atomic protrusions on their surface. The structure displays a rectangular unit cell and is incommensurate with the Pt substrate. The DFT model of Fig. 1.20b is based on a Pt–Ti–O stacking, a Ti_6O_8 stoichiometry, and contains Ti atoms coordinated to four O atoms (labeled as Ti_4) and Ti atoms coordinated to three O atoms (labeled as Ti_3), with a ratio of Ti_4/Ti_3 equal to two. The Ti_4 give rise to the brighter zig-zag contrast whereas the dark

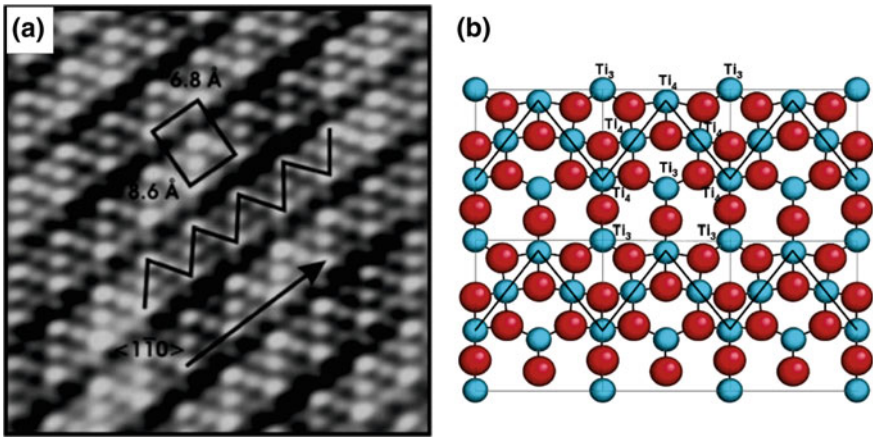

Fig. 1.20 **a** STM image of the TiO_x-zig-zag phase on Pt(111) [(6 × 6 nm^2); V_S = +0.1 V; I_T = 1.5 nA]. **b** Top view of the proposed DFT model (*blue* Ti atoms; *red* O atoms). Adapted from [73] (Color figure online)

troughs are formed by bridging oxygens that connect the Ti_4 and Ti_3 atoms [73]. The DFT analysis of the driving force for the formation of this zig-zag structure motif suggested that the oxide/metal interaction is only weakly directional although important for the stability of the phase, and that the tendency to form a closed-packed hexagonal Ti layer is frustrated by the lack of Ti atoms at the established Ti coverage. Consequently, the Ti atoms arrange themselves into close-packed stripes separated by bridging oxygen atoms. There are two non-equivalent Ti atoms in the stripes, both in terms of O coordination and Pt sites, which cause the different contrast in the STM.

An ordered tungsten oxide monolayer film has been fabricated on Pt(111) by Li et al. [74] using a non-conventional preparation methodology: $(WO_3)_3$ clusters, generated in the gas phase by direct thermal sublimation of WO_3, have been deposited onto the Pt surface and their condensation has been initiated by thermal annealing. The surface induced opening of the $(WO_3)_3$ rings leads to the formation of zig-zag chains, which assemble into a 2-D W oxide wetting layer with a c(4 × 2) superstructure. According to the DFT analysis, the oxide layer is bonded to the Pt surface both via part of the oxygen atoms and by one half of the W atoms, which become reduced to the +5 oxidation state; the latter is in agreement with the signatures in the XPS core level spectra. The other 1/2 of the W atoms remains in the +6 oxidation state and forms tungstyl W=O groups pointing along the surface normal and creating the zig-zag structure that appears in the STM image. The interface layer is slightly buckled and contains both O atoms and W atoms, the latter in 5+ and 6+ oxidation states, whereas the tungstyl oxygens form an open quasi-hexagonal outer surface layer. The c(4 × 2) structure corresponds to a coverage (=W/Pt surface atom) of 0.5; increasing the coverage to form a denser oxide monolayer was investigated at the theoretical level, but was found energetically unfavorable. Instead, the formation of a second layer of clusters on top of the 2-D monolayer sheet has been suggested, and this has indeed been observed experimentally in the form of a (3 × 3) second layer superstructure [74].

The ultrathin layers of alumina that form on Ni–Al alloy single crystal surfaces by selective oxidation may be mentioned in this context of complex oxide structures. Taking the AlO_x double bilayer formed by high temperature oxidation of the Ni_3Al (111) surface as an example, this structure is built up by an Al–O–Al–O stacking sequence, with a complex combination of square and triangular Al–O arrangements at the surface and a hole at the corners of the $(\sqrt{6}7 \times \sqrt{6}7)R12.2°$ unit cell, reaching down to the Ni_3Al substrate interface [75]. The analog oxide layer on NiAl(110) has been rationalized by a similar structure concept, with an $Al_4O_6Al_6O_7$ stoichiometry, O atoms arranged in squares and triangles and Al atoms in between slightly below, but almost coplanar with the oxygen layer [76]. This oxide film also has another O and Al layer at the interface with the substrate. The oxidation of both Ni–Al substrate surfaces is self-limited to the double bilayer AlO_x thickness in the absence of metal impurities. However, the presence of metal nanoparticles on the alumina surface can promote further oxidation and a thickening of the alumina film [77, 78]. This may be of importance and has to be taken into account, if the alumina films are intended to be used as inert substrates for metal particles in model catalyst studies.

1.3 Reactive Interfaces—Ternary Oxides: Increasing the Complexity

If the chemical interactions between the constituents of the interface are strong, interdiffusion can be initiated and eventually a new interfacial compound can be formed, thus creating a so-called reactive interface. The growth of CaO on Mo(001) may be cited as an example [79, 80]. Crystalline Ca oxide films have been prepared after reactive evaporation of Ca in oxygen atmosphere onto a Mo(001) surface followed by annealing to 1000 K. At low film thickness (≤2 ML) a considerable interdiffusion of Mo atoms into the oxide overlayer has been detected by Auger electron spectroscopy, which was accompanied by the formation of a sharp (2 × 2) LEED pattern. With the help of DFT calculations, the oxide phase at the interface has been interpreted as a Ca_3MoO_4 ternary oxide, where 25 % of Ca cations are replaced by Mo in the RS structure [80]. In contrast to CaO, the ternary molybdate has a smaller lattice constant as a result of the smaller size of the Mo cations as compared to Ca cations and consequently a negligible lattice mismatch with the Mo (001) surface: the interdiffusion of Mo and the formation of this ternary phase may therefore be regarded as a chemical means to reduce the interfacial strain. A further driving force for the formation of this mixed oxide has been ascribed to the higher oxygen content of the new phase due to the presence of Mo atoms and to the formation of an oxidized Mo plane at the interface [80].

The concept of the reactive interface has been employed by Denk et al. [81] as an unconventional approach to fabricate ternary metal tungstates at the 2-D limit. A Cu(110) surface with a (2 × 1) surface oxide reconstruction has been covered by a monolayer of cyclic $(WO_3)_3$ clusters, the latter deposited via a molecular beam from the gas phase, and the interfacial chemical reaction has been initiated by temperature treatment at 600 K, as schematically illustrated in Fig. 1.21a. The resulting well-ordered oxide monolayer has been fully characterized experimentally by a combination of diverse surface science techniques and has been interpreted with the help of DFT calculations as a $CuWO_4$ ternary layer. The complex structure model, which is shown in Fig. 1.21b, corresponds to a sequence of three sublayers with stacking O–W–O/Cu from the Cu interface and contains W atoms with a tetrahedral oxygen coordination. This structure is significantly different from the bulk wolframite structure of $CuWO_4$ [83], although the three-layer stacking sequence (O–W–O/Cu) is somewhat reminiscent of the O–W–O–Cu stacking in the wolframite structure, which however contains W with an octahedral oxygen coordination. On the other hand, the scheelite structure, in which other metal tungstates with larger cations crystallize [84, 85], does have a tetrahedral W–O coordination. The 2-D $CuWO_4$ structure on Cu(110) may therefore be regarded somewhat superficially as a combination of wolframite and scheelite structure elements.

The preparation method of $CuWO_4$ as outlined above, namely the surface reaction between a well-ordered 2-D surface oxide and a layer of $(WO_3)_3$ clusters, is

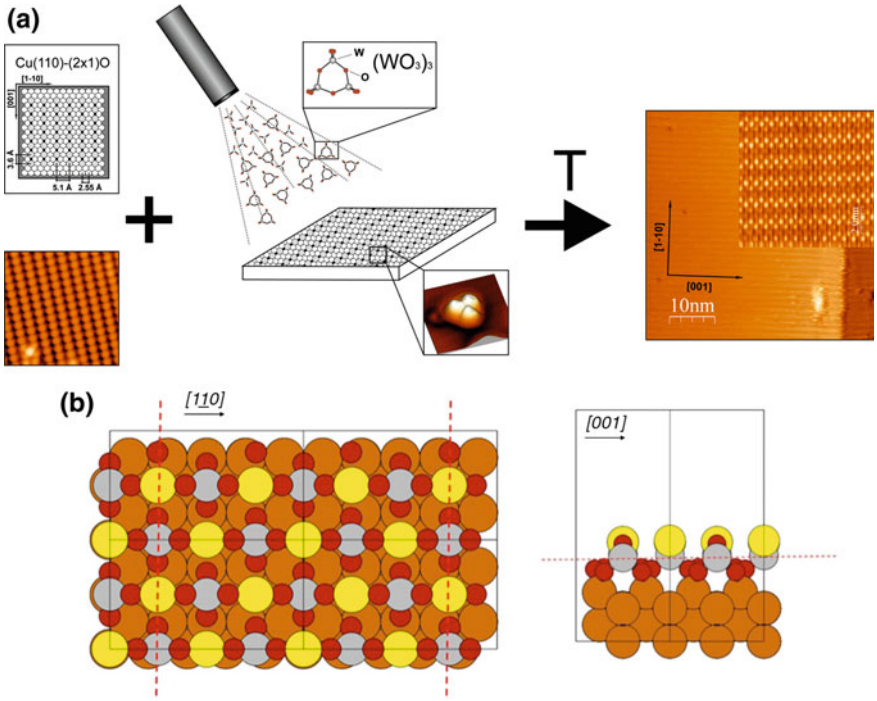

Fig. 1.21 **a** Schematic illustration of the formation of a surface Cu-tungstate phase: a Cu(110) 2 × 1-O surface oxide is covered by $(WO_3)_3$ clusters from the gas phase and an interfacial reaction is initiated by T treatment to yield an ordered $CuWO_4$ layer (*right panel*). **b** DFT derived structure model, *top* and *side views* (*brown* Cu substrate atoms; *grey* W atoms; *red* O atoms; *yellow* Cu atoms in the top surface layer). Adapted from [81, 82]

not particular to the Cu-tungstate phase, but appears to be of a more general validity. For example, Ni-tungstate $NiWO_4$ on Ni(110) has been fabricated by chemical reaction of NiO/Ni(110) with $(WO_3)_3$ clusters [86], and a surface Fe-tungstate phase has been generated by the interfacial reaction of the FeO(111) bilayer phase on Pt(111) (see Sect. 1.2.2) with $(WO_3)_3$ clusters [87]. The first step in the latter interface reaction between FeO(111)/Pt(111) and $(WO_3)_3$ clusters has been observed by Li et al. [88], who found evidence for the dissociation of the clusters into WO_3 monomers in their STM images. The related DFT calculations revealed that the dissociation is accompanied by significant restructuring of the FeO (111), with the Fe ions being pulled on top of the surface and bonded to the WO_3 fragments [88].

1.4 Finite Size Effects

Finite size effects are ubiquitous in nanoscale materials [89–91]. A suitable concept for the investigation of finite size effects in oxide nanostructure research is to use the regular step arrangement of a vicinal metal surface as a model template. Schoiswohl et al. [92] have examined the growth structures of 2-D V oxide layers on a vicinal Rh (15 15 13)Rh(15 15 13) surface and have compared them with those on a flat Rh (111) surface. It was found that while similar V–O building units as on the Rh(111) surface develop as a function of the chemical potential of oxygen on the (111) terraces of the vicinal Rh surface, the effects of limited terrace size and strain relief at the step edges lead to a rearrangement of building blocks and the stabilization of novel oxide structures that are not observed on the extended (111) surface [92].

A striking consequence of finite size effects has been encountered during the growth of Mn-oxide on a Pd(1 1 17)Pd(1 1 17) surface [93], a vicinal of Pd(100). We recall that on Pd(100) a Mn_3O_4 c(4 × 2) monolayer is formed [26], in which the creation of Mn vacancies in the c(4 × 2) array provides a means to relax interfacial strain (see Sect. 1.2.1). The strain relief in the c(4 × 2) Mn-oxide layer is however incomplete, and the Mn_3O_4 phase on Pd(100) is a domain structure, characterized by relatively small ordered c(4 × 2) domains separated by disordered domain boundaries [94]; the latter obviously are a consequence of strain relief. On Pd(1 1 17), however, a perfectly ordered c(4 × 2) Mn_3O_4 monolayer surface has been obtained, with the step-terrace structure of the vicinal surface in a perfect superlattice (see Fig. 1.22) [93, 95]. The latter is not the case on the clean Pd(1 1 17) surface, where the step-terrace structure is much less regular: the Mn-oxide overlayer obviously stabilizes a regular step-terrace arrangement of the Pd substrate. The quantitative evaluation of the superlattice parameters of this surface by spot-profile analysis LEED (SPA-LEED) yielded a surprising result: the Pd(1 1 17) surface had undergone a massive reconstruction and had rearranged into a Pd(1 1 21) surface under the influence of the c(4 × 2) Mn_3O_4 oxide overlayer growth [93]. DFT calculations elucidated the physical origin of the stabilization mechanism of particular terrace sizes in terms of "magic widths" of the Mn_3O_4 stripes, with particular stable oxide stripes occurring if full c(4 × 2) unit cells can be accommodated on the Pd terraces. The structural details of the most stable $Mn_{14}O_{20}$/Pd(1 1 21) nanostripe showed substantial relaxation and a buckling of the oxide layer at the boundaries, i.e. at the step edges, which is a clear consequence of limited size effects [93, 95].

1.5 Interface Chemistry

The strong chemical affinities between the elements constituting the interface are at the root of the reactive interface formation, as discussed in Sect. 1.3. Here we will include the affinity to oxygen and examine, how these affinities reflect on the type of particular oxide structure formed on different metal substrates. Prototypical

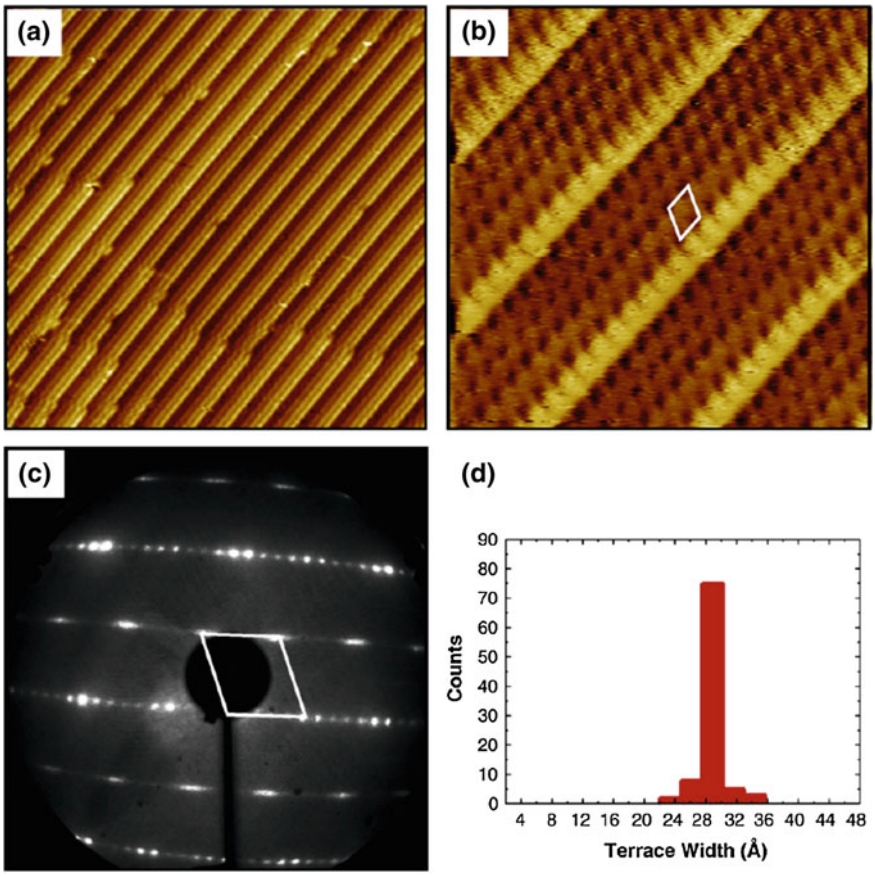

Fig. 1.22 **a**, **b** STM images of the c(4 × 2) Mn-oxide/Pd(1 1 21) surface (**a** (40 × 40 nm^2); V_S = +1.5 V; I_T = 0.1 nA; **b** (10 × 10 nm^2); V_S = −0.2 V; I_T = 0.1 nA); a primitive c(4 × 2) unit cell is indicated in (**b**). **c** LEED pattern of the c(4 × 2) surface (electron energy = 120 eV). **d** Terrace width distribution of the c(4 × 2) oxide surface. Reproduced with permission from [95]

examples are difficult to find, because the chemical effects are in general strongly mixed up with elastic and electronic effects, so that the chemistry, as defined here, is difficult to single out. A few systems, however, may be discussed in terms of showing these interface chemistry aspects.

The highly oxidized V-oxide monolayers show a (4 × 4) structure on Pd(111) and a ($\sqrt{7} \times \sqrt{7}$)R19.1° structure on Rh(111) surfaces, which are formed by different V–O coordination units and somewhat different stoichiometries. The (4 × 4) structure on Pd(111) is an open network structure of VO_4 units with tetrahedral V–O coordination and a formal $VO_{2.8}$ stoichiometry, whereas the ($\sqrt{7} \times \sqrt{7}$)R19.1° structure on Rh(111) is built up by quadratic VO_5 pyramids with a formal VO_3 stoichiometry [96]. It is noted that the (4 × 4) V-oxide is thus only slightly O

deficient with respect to the $(\sqrt{7} \times \sqrt{7})$R19.1° phase. Closer inspection of the proposed structure models shows, however, that the interface of the $(\sqrt{7} \times \sqrt{7})$R19.1° structure is considerably denser in oxygen: the pyramidal VO_5 units of the $(\sqrt{7} \times \sqrt{7})$R19.1° structure are attached to the Rh surface via four oxygen atoms of their basal plane, whereas the tetrahedral VO_4 units of the (4 × 4) phase are bonded alternately via only one or two oxygen atoms to the Pd substrate. The difference in surface lattice constants beween Rh(111) and Pd(111) is relatively small (∼2.2 %), so that the elastic strain is unlikely to be the decisive factor in determining these different oxide structures. It has been proposed that the higher affinity of Rh towards oxygen may be the cause for the structural difference of these highly oxidized V-oxide structures on Rh(111) and Pd(111) substrate surfaces [96]; this is an interface chemistry effect in the sense discussed here.

The Co-oxide monolayer grows on Ir(100) in a c(10 × 2) structure, which has been interpreted in terms of a hexagonal RS (111)-type bilayer [97] (see Sect. 1.2.2). The Co-oxide monolayer however displays a different structure, if the substrate is chemically modified by deposition of a pseudomorphic Co monolayer as an interlayer on top of the Ir(100) surface: in this latter case, an RS (100)-like c (4 × 2) Co_3O_4 vacancy structure is formed [98] (see Sect. 1.2.1). Gubo et al. have analyzed the stability of the two systems by ab initio thermodynamic phase diagrams and found that, while the c(10 × 2) structure is thermodynamically most stable over a wide range of oxygen chemical potentials on the bare Ir(100) surface, the c(4 × 2) structure becomes more stable on the Co/Ir(100) support. The strength of the interface chemical bonding between the oxide oxygen and the Co atoms of the support interlayer has been made responsible for the formation of this c(4 × 2) oxide structure [98]; in the latter structure, the overlayer-substrate bonding appears to be more specific and directional than in the c(10 × 2) phase, which is less commensurate.

The first monolayer of W-oxide on Pt(111), displaying a c(4 × 2) structure with zig-zag line motif of W–O chains condensed into a 2-D network, is anchored to the Pt surface by strong W–Pt and O–Pt bonds [74]. In contrast, W-oxide on Ag(100) forms an extended first wetting layer with square symmetry that is incommensurate to the substrate: this creates a characteristic Moiré modulation pattern in the STM images [21]. The interesting aspect of this W-oxide monolayer is that it is rotationally disordered in different domains, that is the registry of the WO_x layer is in a random azimuth orientation with respect to the Ag(100) surface directions; this becomes apparent from a varying Moiré signature in different domains, but is also most simply seen in the LEED pattern. Figure 1.23 shows a LEED pattern of the WO_x/Ag(100) surface: the bright outer spots are the integer order reflections of the Ag substrate, whereas the weak ring-like intensity is from the rotationally disordered domains of the WO_x overlayer. There are indications that there is some preferential orientation of domains rotated 45° with respect to Ag(100) surface lattice, but the rotational disorder is clearly apparent. Although the exact atomic structure of the WO_x monolayer on Ag(100) has not yet been resolved, the

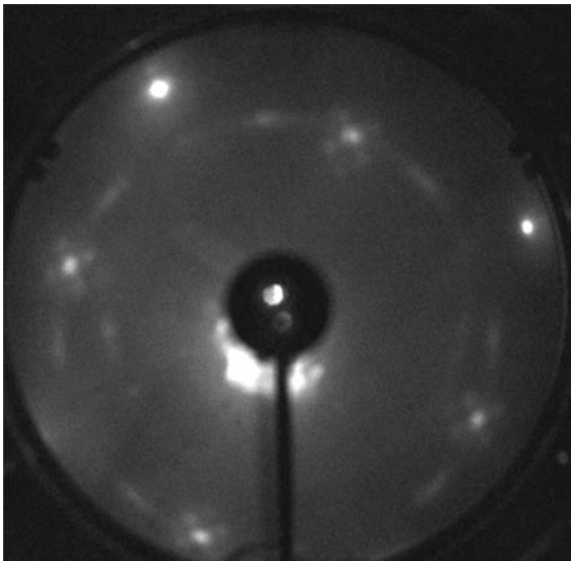

Fig. 1.23 LEED pattern of the WO_x monolayer phase on Ag(100) (electron energy = 66 eV). The bright outer spots are the integer order reflections of the Ag (100) substrate, the weak ring-like intensity is from the first order reflections of the rotationally disordered overlayer. Adapted from [21]

orientational randomness of the WO_x overlayer indicates that the surface potential is flat and that the chemical interactions across the interface are not pronounced. This is in line with the weak chemical affinitiy of silver to tungsten and oxygen.

1.6 Surface Phase Diagrams

Elements with several atomic oxidation states of comparable stability may exhibit a very complex oxide structure behavior as a function of external growth parameters, and an impression of such structural complexities may be obtained from the surface phase diagram. The term is used here as the projection of the regions of stable phases onto the relevant parameter space, which is in most cases the chemical potential of oxygen μ_O and the metal atom surface concentration as expressed by the surface coverage; notice that the metal atom surface concentration not only determines the actual oxide coverage of the surface, but also influences the stoichiometry of the growing oxide phase due to kinetic effects. This definition of phase diagram is different from the one in the thermodynamic sense, where the total energy of a phase versus a particular parameter, e.g. μ_O, is presented. Complex phase diagrams have been reported for V-oxides on Pd(111) [50] or Rh(111) [68, 72] surfaces, Ti-oxides on Pt(111) [55, 56], or Mn-oxides on Pd(100) [94]. The latter is a benchmark system and the surface phase diagram for a given metal coverage as a function of μ_O is illustrated in Fig. 1.24. Nine different 2-D Mn-oxide phases have been detected as a function of μ_O. The phases in the different regions of the μ_O (e.g. “oxygen-rich”, etc.) are structurally related to each other and often occur in coexistence at the surface. It should be mentioned at this point that the latter constitutes a considerable problem for the experimental characterization of the

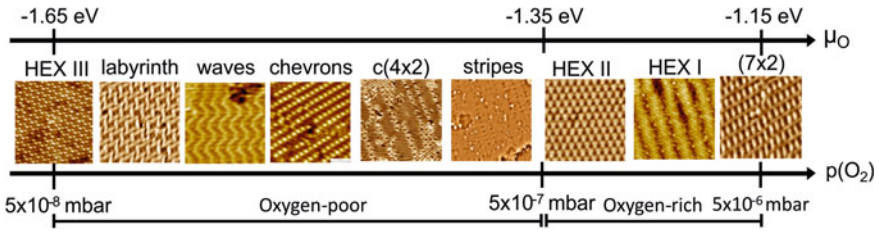

Fig. 1.24 Schematic phase diagram of 2-D Mn-oxides on Pd(100), presented as a function of the oxygen pressure p_{O2} and of the oxygen chemical potential μ_O. The nominal coverage of Mn on the surface is 0.75 ML. Adapted from [94]

different phases, since subtle variations in the thermodynamic parameters, often below the control of the experimenter, may drive the system into a different structure. It is therefore a challenge in these systems with multi-structure phase diagrams to reproducibly prepare a particular phase, which sometimes even cannot be prepared as a single phase at the surface. This is detrimental for the structure characterization, since a combination of several experimental techniques is often necessary, including area averaging techniques besides the space-resolved STM, to unravel a complex oxide structure. In the "oxygen-rich" regime of the MnO_x/Pd (100) phase diagram (Fig. 1.24), hexagonal trilayer MnO_2-type structures are observed (Sect. 1.2.2), in the "intermediate" region the c(4 × 2) Mn_3O_4 phase is central (Sect. 1.2.1), with the other phases related to it by a vacancy propagation mechanism [5, 29], whereas in the "oxygen-poor" region (left part of the diagram), the atomic details of the reduced structures are mostly lacking for the reasons mentioned above.

The importance of kinetic stabilization in surface oxide phase diagrams cannot be underestimated—see the discussion of Fortunelli et al. in Chap. 2. It appears that kinetic effects in 2-D systems are more prominent than in 3-D bulk systems. This may be related to the enhanced flexibility of 2-D oxide structures in terms of geometric stiffness, which depends on the O-coordination number [2]—with less flexibility for higher O-coordination—as well as in terms of allowing for different metal-oxygen building blocks and their variable connectivities.

1.7 Pattern Formation

The mismatch of lattice constant and symmetry across a hetero-epitaxial interface may lead to the formation of a mesoscopic corrugation pattern at the surface. This has been demonstrated for a nanostripe pattern of a NaCl monolayer on a Cu(110) surface [99]. NaCl is not an oxide, but a dielectric material, and similar effects are expected to occur on other 2-D dielectric systems, including oxides. Indeed, very recently the formation of a nanostripe pattern has been observed for a 2-D layer of CeO_2 on Cu(110) [100]. NaCl grows in the form of quadratic RS (100) monolayers

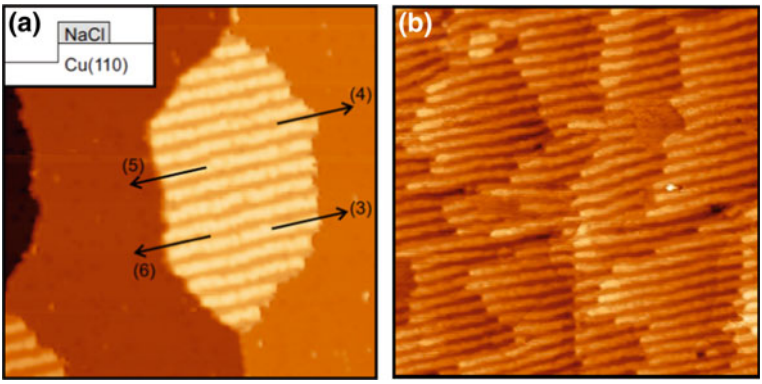

Fig. 1.25 **a** STM image of a NaCl monolayer island on Cu(110) located at an upper step edge (as illustrated by the cartoon in the *insert*) [(81 × 81 nm^2); $V_S = -1.75$ V; $I_T = 0.03$ nA]. **b** STM image of 1 ML NaCl on Cu(110) [(111.5 × 115.5 nm^2); $V_S = +1.0$ V; $I_T = 0.1$ nm]. Adapted from [99]

on Cu(110), as on most other noble metal surfaces. Figure 1.25a shows an STM image of an individual NaCl island at a step edge, and Fig. 1.25b of the full NaCl monolayer on Cu(110): the pattern of dark and bright stripes with a periodicity distance of ∼40 Å and a corrugation of ∼1.2 Å is clearly apparent. The formation of this pattern has been interpreted with the help of DFT calculations as the result of the frustration of the overlayer-substrate chemical bonding produced by the epitaxial mismatch. In regions of a favorable epitaxial relationship the Cu–Cl covalent bonding is strong and the overlayer-substrate distance is short; conversely, in regions of poor epitaxial match the Cu–Cl bonding is weak and the overlayer-substrate distance is long. This leads to a chemically induced periodic modulation of the overlayer topography and a geometric rumpling of the surface, and thus to the observed stripe pattern in the STM. This is a true 2-D effect: simulations of NaCl bilayers were conducted, but the experimental corrugation could not be reproduced, because the interaction of the first interfacial NaCl layer with the second NaCl layer competes with that with the support, reducing substantially the topographic corrugation at the surface [99]. The formation of such anisotropic template surfaces, produced by the epitaxial lattice and symmetry mismatch in a hetero-epitaxial 2-D dielectric-metal system, may be of interest for the growth of hierarchical superstructures or for the engineering of periodic strain on oxide surfaces [100], with associated heterogeneous surface properties.

1.8 Synopsis

Oxide materials at the 2-D limit, supported on metal surfaces, exhibit a fascinating, sometimes confusing complexity of geometries and phases. We have analyzed this structural behavior of 2-D oxides with the aim to understand and reduce the

complexity by tracing down common structure motifs and trends. To identify the physical origin driving oxide phases into a particular structure and atomic geometry, we have attempted to isolate the major physical parameters that drive a system into a particular phase, employing a reductionist approach. This is, of course, somewhat simplistic, since the various degrees of freedom—geometric, electronic, chemical, magnetic—are intimately coupled and interwoven. However, it is a useful approach for a categorical discussion and of pedagogical advantage.

To categorize oxide structures, we have chosen either a stacking layer representation, e.g. using a sequence of oxygen and metal layers, or a description by combining and nesting the individual M–O coordination building blocks, the selection being made somewhat arbitrarily with the purpose of easy perception. A variety of structure concepts have been identified and their characteristic parameters have been discussed. To illustrate the major oxide structure categories, benchmark systems have been chosen for the presentation. The main body of this chapter has been devoted to describe and analyze structure types of binary oxide systems, where most of the surface science based work has been undertaken hitherto, but the way towards more complex ternary oxide systems has been indicated.

Interfaces play an important role in hetero-epitaxial thin film growth. The more so for the behavior of 2-D overlayers, where the parameters of the interface become decisive in determining the properties of the whole system. The geometry and the electronic/chemical interactions at the interface have therefore been emphasized throughout the treatise as a major structure determining aspect. Finite size effects are present in all nanoscale systems, but are particularly prominent at low dimensionality. In this context, we have investigated the consequence of the steps of vicinal metal substrate surfaces for the formation of oxide overlayers and their influence on the stability of structures. The interplay of thermodynamic and kinetic effects is responsible for the structural richness of some oxide surface phase diagrams, where several different phases can coexist at the surface after preparation under closely related conditions. Such multitude of oxide structures of similar stability may be regarded as a structurally degenerated ground state, which is conceptually interesting because it illustrates most evidently the flexibility of structure building blocks of oxides at the 2-D limit. Experimentally, it is difficult to handle, since area averaging techniques cannot be applied. The epitaxial lattice and symmetry misfit at the interface between a metal and a dielectric layer may give rise to the formation of a periodic anisotropy at the surface of oxides and the spontaneous appearance of mesoscopic stripe patterns. This supports the notion of a local chemical bonding concept at the interface, as the stripe pattern has been ascribed to the frustration and the local variation of the interfacial bonding due to the epitaxial mismatch.

The study of structures of 2-D oxide systems, which span the range from a single plane of a bulk crystal to novel structure types containing unusual metal oxidation states in metal-oxygen coordination spheres with atypical connectivities, has been an evolving field of research during the last one and a half decades that has benefitted enormously from the progress in area-resolving experimental methodologies (e.g. the scanning probe techniques) and advanced density functional theory techniques (see the Chap. 2 by Fortunelli et al.). It was the close combination of

experiment and theory that has enabled the remarkable advances in this field and has led to an atomic picture of very complex oxide phases, and a glimpse of this close coupling between experiment and theory has been given in this chapter. Due to the concentration on structure aspects, local probe techniques have been in the foreground of the present description, but the connection with complementary area averaging techniques, e.g. electron spectroscopies, has been crucial for the progress in the field.

What are the further perspectives for the years to come? The path towards more complexity is already preordained and the study of ternary oxides and beyond is on the way. The magnetic structures of 2-D oxides have been addressed during their theoretical modeling, but experimental investigations are still sparse; we expect more to come. Most studies of 2-D oxides have been performed on systems supported on metal surfaces; the structure of 2-D oxides on oxide substrates is largely unexplored. In view of their high interest in catalytic chemistry, 2-D oxide systems supported on oxides substrates are an emerging active area of research. The combination of 2-D oxides with other 2-D materials (e.g. oxides supported on graphene, BN and the like) has been barely attempted so far. Such combinations may be of interest from the point of view of weakly interacting systems, where the intrinsic 2-D oxide character may be preserved due to the expected weaker influence of the interface to the substrate. The materials science of 2-D oxides is a wide open field and we expect new phenomena and materials′ properties to be discovered.

Acknowledgement FPN acknowledges financial support from the ERC Advanced Grant "Search for emergent properties of oxide nanostructures" (SEPON) and from the University of Graz. SS is supported by the FWF (P26633-N20).

References

1. Pacchioni G, Valeri S (eds) (2012) Oxide ultrathin films: science and technology. Wiley-VCH, Weinheim
2. Freysoldt C, Rinke P, Scheffler M (2007) Ultrathin oxides: bulk-oxide-like model surfaces of unique films? Phys Rev Lett 99:086101
3. Butler SZ, Hollen SM, Cao L et al (2013) Progress, challenges, and opportunities in two-dimensional materials beyond graphene. ACS Nano 4:2898–2926
4. Netzer FP, Allegretti F, Surnev S (2010) Low-dimensional oxide nanostructures on metals: hybrid systems with novel properties. J Vac Sci Technol B 28:1–16
5. Surnev S, Fortunelli A, Netzer FP (2013) Structure-property relationship and chemical aspects of oxide-metal hybrid nanostructures. Chem Rev 113:4314–4372
6. Netzer FP (2010) "Small and beautiful"—the novel structues and phases of nano-oxides. Surface Sci 604:485–489
7. Campbell CT (2006) Transition metal oxides: extra thermodynamic stability as thin films. Phys Rev Lett 96:066106
8. Valeri S, Benedetti S (2012) Synthesis and preparation of oxide ultrathin films. In: Pacchioni G, Valeri S (eds) Oxide ultrathin films: science and technology. Wiley-V-CH, Weinheim, pp 1–26

9. Grinter DC, Thornton G (2012) Characterization tools of ultrathin oxide films. In: Pacchioni G, Valeri S (eds) Oxide ultrathin films: science and technology. Wiley-V-CH, Weinheim, pp 27–46
10. Pacchioni G (2012) Two-dimensional oxides: multifunctional materials for advanced technologies. Chem Eur J 18:10144–10158
11. Tasker PW (1979) The stability of ionic crystal surfaces. J Phys C: Solid State Phys 12:4977–4984
12. Goniakowski J, Finocchi F, Noguera C (2008) Polarity of oxide surfaces and nanostructures. Rep Prog Phys 71:016501
13. Lüth H (1993) Surfaces and interfaces of solids. springer series in surface sciences 15, Springer, Berlin
14. Brune H (1998) Microscopic view of epitaxial metal growth: nucleation and aggregation. Surf Sci Rep 31:121–230
15. Pauling L (1947) Atomic radii and interatomic distances in metals. J Am Chem Soc 69:542–553
16. Thomas IO, Fortunelli A (2010) Analysis of the electronic structure of ultrathin NiO/Ag(100) films. Eur Phys J B75:5–13
17. Barcaro G, Thomas IO, Fortunelli A (2010) Validation of density-functional versus density-functional + U approaches for oxide ultrathin films. J Chem Phys 132:124703
18. Steurer W, Allegretti F, Surnev S et al (2011) Metamorphosis of ultrathin Ni oxide nanostructures on Ag(100). Phys Rev B 84:115446
19. Steurer W, Surnev S, Fortunelli A, Netzer FP (2012) Scanning tunneling microscopy imaging of Ni(100)1 × 1 islands embedded in Ag(100). Surface Sci 606:803–807
20. Obermüller T, Steurer W, Surnev S et al (2013) Kinetic asymmetry in the growth of two-dimensional Mn oxide nanostripes. Phys Rev B 88:235410
21. Obermüller T (2015) Growth of transition metal oxides in 2D layers: probing and tuning the properties of matter at the atomic scale. PhD thesis, University of Graz
22. Müller F, de Masi R, Reinicke DK et al (2002) Epitaxial growth of MnO/Ag(001) films. Surface Sci 520:158–172
23. Schoiswohl J, Agnoli S, Xu B et al (2005) Growth and thermal behaviour of NiO nanolayers on Pd(100). Surface Sci 599:1–13
24. Agnoli S, Sambi M, Granozzi G et al (2005) Experimental and theoretical study of a surface stabilized monolayer phase of nickel oxide on Pd(100). J Phys Chem B 109(17197):17204
25. Allegretti F, Parteder G, Gragnaniello L et al (2010) Strained c(4 × 2) CoO(100)-like monolayer on Pd(100): experiment and theory. Surface Sci. 604:528–533
26. Franchini C, Zabloudil J, Podloucky R et al (2009) Interplay between magnetic, electronic, and vibrational effects in monolayer Mn_3O_4 grown on Pd(100). J Chem Phys 130:124707
27. Fortunelli A (2015), private communication
28. Gragnaniello L, Agnoli S, Parteder G et al (2010) Cobalt oxide nanolayers on Pd(100): the thickness-dependent structural evolution. Surface Sci 604:2002–2011
29. Franchini C, Podloucky R, Allegretti F et al (2009) Structural and vibrational properties of two-dimensional Mn_xO_y layers on Pd(100): experiments and density functional calculations. Phys Rev B 79:035420
30. Altieri S, Allegretti F, Steurer W et al (2013) Orbital anisotropy in paramagnetic manganese oxide nanostripes. Phys Rev B 87:241407(R)
31. Goniakowski J, Noguera C, Giordano L (2004) Using polarity for engineering oxide nanostructures: structural phase diagram in free and supported MgO(111) ultrathin films. Phys Rev Lett 93:215702
32. Kiguchi M, Entani S, Saiki K et al (2003) Atomic and electronic structure of an unreconstructed polar MgO(111) thin film on Ag(111). Phys Rev B 68:115402
33. Tusche C, Meyerheim HL, Kirschner J (2007) Observation of depolarized ZnO(0001) monolayers: formation of unreconstructed planar sheets. Phys Rev Lett 99:026102
34. Weirum G, Barcaro G, Fortunelli A et al (2010) Growth and surface structure of zink oxide layers on a Pd(111) surface. J Phys Chem C114:15432–15439

35. Parteder G, Allegretti F, Wagner et al (2008) Growth and oxidation of Ni nanostructures on stepped Rh surfaces. J Phys Chem C112:19272–19278
36. Franz T, Zabloudil J, Mittendorfer F et al (2012) Deformed surface oxides: uncommon structure of a (6 × 1) NiO surface oxide on Rh(111). J Phys Chem Lett 3:186–190
37. Hagenbach Ch, Shantyr R, Neddermeyer H et al (2006) Pressure-dependent Ni-O phase transitions and Ni oxide formation on Pt(111): an in situ STM study at elevated temperatures. Phys Chem Chem Phys 8:1575–1583
38. Galloway HC, Benitez JJ, Salmeron M (1994) Growth of FeO_x on Pt(111) studied by tunneling microscopy. J Vac Sci Technol, A 12:2302–2307
39. Galloway HC, Sautet P, Salmeron M (1996) Structure and contrast in scanning tunneling microscopy of oxides: FeO monolayer on Pt(111). Phys Rev B 54:R11145–R11148
40. Kim YJ, Westphal C, Ynzunza RX et al (1997) Interlayer interactions in epitaxial oxide growth: FeO on Pt(111). Phys Rev B 55:R13448–R13451
41. Ritter M, Ranke W, Weiss W (1998) Growth and structure of ultrathin FeO films on Pt(111) studied by STM and LEED. Phys Rev B 57:7240–7251
42. Ranke W, Ritter M, Weiss W (1999) Crystal structures and growth mechanism for ultrathin films of ionic compound materials: FeO(111) on Pt(111). Phys Rev B 60:1527–1530
43. Weiss W, Ranke W (2002) Surface chemistry and catalysis on well-defined epitaxial iron-oxie layers. Progr Surface Sci 70:1–151
44. Zeuthen H, Kudernatsch W, Peng G et al (2013) Structure and stoichiometry of oxygen-rich ultrathin FeO(111) films grown on Pd(111). J Phys Chem C117:15155–15163
45. Shaikhutdinov Sh, Ritter M, Weiss W (2000) Hexagonal heterolayers on a square lattice: a combined STM and LEED study of FeO(111) on Pd(100). Phys Rev B 62:7535–7541
46. Kuhness D (2015) Synthesis of low dimensional ternary oxide $FeWO_x$ and $MnWO_x$ nanostructures on single crystal metal surfaces. PhD thesis, University of Graz
47. Ebensperger C, Gubo M, Meyer W et al (2010) Substrate-induced structural modulation of a CoO(111) bilayer on Ir(100). Phys Rev B 81:235405
48. Gragnaniello G, Barcaro G, Sementa L et al (2011) The two-dimensional cobalt oxide (9x2) phase on Pd(100). J Chem Phys 134:184706
49. Surnev S, Vitali L, Ramsey MG et al (2000) Growth and structure of ultrathin vanadium oxide layers on Pd(111). Phys Rev B 61:13945–13954
50. Surnev S, Kresse G, Ramsey MG et al (2001) Novel interface-mediated metastable oxide phases: vanadium oxides on Pd(111). Phys Rev Lett 87:86102
51. Kresse G, Surnev S, Ramsey MG et al (2001) First-principles calculations for V_xO_y grown on Pd(111). Surface Sci 492:329–344
52. Sambi M, Petukhov M, Domenichini B et al (2003) A photoelectron diffraction study of the surface-V_2O_3 (2 × 2) layer on Pd(111). Surface Sci 529:L234–L238
53. Surnev S, Kresse G, Sock M et al (2001) Surface structures of ultrathin vanadium oxide films on Pd(111). Surface Sci 495:91–196
54. Surnev S, Sock M, Kresse G et al (2003) Unusual CO adsorption sites on vanadium oxide—Pd(111) "inverse model catalyst" surfaces. J Phys Chem B 107:4777–4785
55. Sedona F, Rizzi GA, Agnoli S et al (2005) UltrathinTiO_x films on Pt(111): A LEED, XPS, and STM investigation. J Phys Chem B 109:24411–24426
56. Barcaro G, Agnoli S, Sedona F et al (2009) Structure of reduced ultrathin TiO_x polar films on Pt(111). J Phys Chem C113:5721–5729
57. Reuter K, Stampfl C, Ganduglia-Pirovano MV et al (2002) Atomistic description of oxide formation on metal surfaces: the example of ruthenium. Chem Phys Lett 352:311–317
58. Gustafson J, Mikkelsen A, Borg M et al (2004) Self-limited growth of a thin oxide layer on Rh(111). Phys Rev Lett 92:126102
59. Heinz K, Hammer L (2013) Epitaxial cobalt oxide films on Ir(100)—the importance of crystallographic analyses. J Phys: Condens Matter 25:173001
60. Giordano L, Lewandowski M, Groot IMN et al (2010) Oxygen-induced transformations of an FeO(111) film on Pt(111): a combined DFT and STM study. J Phys Chem C114:21504–21509

61. Sun YN, Giordano L, Goniakowski J et al (2010) The interplay between structure and CO oxidation catalysis on metal-supported ultrathin oxide films. Angew Chem Int Ed 49:4418–4421
62. Lewandowski M, Groot IMN, Shaikhutdinov S et al (2012) Scanning tunneling microscopy evidence for the Mars-van Krevelen type mechanism of low temperature CO oxidation on an FeO(111) film on Pt(111). Catal Today 181:52–55
63. Eck S, Castellarin-Cudia C, Surnev S et al (2002) Growth and thermal properties of ultrathin cerium oxide layers on Rh(111). Surface Sci 520:173–185
64. Castellarin-Cudia C, Surnev S, Schneider G et al (2004) Strain-induced formation of arrays of catalytically active sites at the metal-oxide interface. Surface Sci. 554:L120–L126
65. Lu J-L, Gao H-J, Shaikhutdinov S et al (2006) Morphology and defect structure of the CeO_2(111) films grown on Ru(0001) as studied by scanning tunneling microscopy. Surface Sci. 600:5004–5010
66. Staudt T, Lykhach Y, Hammer L et al (2009) A route to continuous ultra thin cerium oxide films on Cu(111). Surface Sci. 603:3382–3388
67. Grinter DC, Ithnin R, Pang CL et al (2010) Defect structure of ultrathin ceria films on Pt (111): atomic views from scanning tunneling microscopy. J Phys Chem C114:17036–17041
68. Schoiswohl J, Sock M, Eck S et al (2004) Atomic-level growth study of vanadium oxide nanostructures on Rh(111). Phys Rev B 69:155403
69. Klein C, Kresse G, Surnev S et al (2003) Vanadium surface oxides on Pd(111): a structural analysis. Phys Rev B 68:235416
70. Schoiswohl J, Surnev S, Netzer FP (2006) Vanadium oxide nanostructures: from zero- to three-dimensional. J Phys: Condens Matter 18:R1–R14
71. Schoiswohl J, Surnev S, Netzer FP (2005) Reactions on inverse model catalyst surfaces: atomic views by STM. Topics Catal 36:91–105
72. Schoiswohl J, Surnev S, Sock M et al (2005) Reduction of vanadium-oxide monolayer structures. Phys Rev B 71:165437
73. Barcaro G, Sedona F, Fortunelli A et al (2007) Structure of a TiO_x zigzag-like monolayer on Pt(111). J Phys Chem C111:6095–6102
74. Li Z, Zhang Z, Kim YK et al (2011) Growth of ordered ultrathin tungsten oxide films on Pt (111). J Phys Chem C115:5773–5783
75. Schmid M, Kresse G, Buchsbaum A et al (2007) Nanotemplate with holes: ultrathin alumina on Ni_3Al(111). Phys Rev Lett 99:196104
76. Kresse G, Schmid M, Napetschnig E et al (2005) Structure of the ultrathin aluminum oxide film on NiAl(110). Science 308:1440
77. Gragnaniello L, Ma T, Barcaro G et al (2012) Ordered arrays of size-selected oxide nanoparticles. Phys Rev Lett 108:195507
78. Chaudhury A, Gragnaniello L, Ma T et al (2013) Alumina-supported array of Co nanoparticles: size-dependent oxidation kinetics? J Phys Chem C117:18112–18119
79. Shao X, Myrach P, Nilius N et al (2011) Growth and morphology of calcium-oxide films grown on Mo(001). J Phys Chem C115:8784–8789
80. Shao X, Nilius N, Myrach P et al (2011) Strain-induced formation of ultrathin mixed-oxide films. Phys Rev B 83:245407
81. Denk M, Kuhness D, Wagner M et al (2014) Metal tungstates atthe ultimate two-dimensional limit: fabrication of a $CuWO_4$ nanophase. ACS Nano 8:3947–3954
82. Ma L, Denk M, Kuhness D et al (2015) Chemical properties of two-dimensional oxide systems: adsorption of $(WO_3)_3$ clusters on $CuWO_4$. Surface Sci. doi:10.1016/j.susc.2015.03.006
83. Kihlborg L, Gebert E (1970) $CuWO_4$, a distorted wolframite-type structure. Acta Cryst B26:1020–1026
84. Zhang Y, Holzwarth NAW, Williams RT (1998) Electronic band structures of the scheelite materials $CaMoO_4$, $CaWO_4$, $PbMoO_4$, and $PbWO_4$. Phys Rev B 57:12738–12750
85. Kuzmin A, Purans J (2001) Local atomic and electronic structure pf tungsten ions in AWO_4 crystals of scheelite and wolframite types. Radiat Meas 33:583–586

86. Pomp S (2013) Interaction of $(WO_3)_3$ clusters with bare Ni(110) and oxygen reconstructed O-Ni(110) surfaces. Master Thesis, University of Graz
87. Pomp S, Kuhness D, Barcaro G, Sementa L, Mankad V, Fortunelli A, Sterrer M, Netzer FP, Surnev S (2016) Two-dimensional iron tungstate: a ternary oxide with honeycomb geometry. Submitted for publication
88. Li S-C, Li Z, Zhang Z et al (2012) Preparation, characterization, and catalytic properties of tungsten trioxide cyclic trimers on FeO(111)/Pt(111). J Phys Chem C116:908–916
89. Huang WJ, Sun R, Tao J et al (2008) Coordination-dependent surface atomic contraction in nanocrystals revealed by coherent diffraction. Nat Mat 7:308–313
90. Mironets O, Meyerheim HL, Tusche C et al (2008) Direct evidence for mesoscopic relaxations in cobalt nanocrystals on Cu(001). Phys Rev Lett 100:096103
91. Feng W, Meyerheim HL, Mohseni K et al (2013) Misfit-induced modification of structure and magnetism in O/Fe(001)-p(1x1). Phys Rev Lett 110:235503
92. Schoiswohl J, Surnev S, Netzer FP (2007) Vanadium oxide overlayers on vicinal Rh(15 15 13): the influence of surface steps. J Phys Chem C111:10503–10507
93. Franchini C, Li F, Surnev S et al (2012) Tailor-made ultrathin manganese oxide nanostripes: "Magic widths" on Pd(1 1 N) terraces. J Phys: Condens Matter 24:042001
94. Li F, Parteder G, Allegretti et al (2009) Two-dimensional manganese oxide nanolayers on Pd (100): the surface phase diagram. J Phys: Condens Matter 21:134008
95. Li F, Allegretti F, Surnev S et al (2010) Atomic engineering of oxide nanostructure superlattices. Surface Sci 604:L43–L47
96. Schoiswohl J, Sock M, Chen Q et al (2007) Metal supported oxide nanostructures: model systems for advanced catalysis. Topics Catal 46:137–149
97. Ebensperger C, Gubo M, Meyer W et al (2010) Substrate-induced structural modulation of a CoO(111) bilayer on Ir(100). Phys Rev B 81:235405
98. Gubo M, Ebensperger C, Meyer W et al (2012) Tuning the growth orientation of epitaxial films by interface chemistry. Phys Rev Lett 108:066101
99. Wagner M, Negreiros FR, Sementa L et al (2013) Nanostripe pattern of NaCl layers on Cu (110). Phys Rev Lett 110:216101
100. Ma L, Doudin N, Surnev S et al (2015) Ceria on Cu(110): formation of nanostripe strain defects. Unpublished results

http://www.springer.com/978-3-319-28330-2

Oxide Materials at the Two-Dimensional Limit
Netzer, F.P.; Fortunelli, A. (Eds.)
2016, XVII, 389 p. 201 illus., 65 illus. in color.,
Hardcover
ISBN: 978-3-319-28330-2